Analysis and Proof-of-principle Implementation of a Laser Doppler Vibrometry based Middle Ear Microphone

Stijn Meersman

Promotoren: prof. dr. ir. Roel Baets, dr. ir. Danae Delbeke
Begeleider: Yanlu Li

Masterproef ingediend tot het behalen van de academische graad van
Master in de ingenieurswetenschappen: fotonica

Vakgroep Informatietechnologie
Voorzitter: prof. dr. ir. Daniël De Zutter
Faculteit Ingenieurswetenschappen
Academiejaar 2009-2010

UNIVERSITEIT
GENT

Analysis and Proof-of-principle Implementation of a Laser Doppler Vibrometry based Middle Ear Microphone

Stijn Meersman

Promotoren: prof. dr. ir. Roel Baets, dr. ir. Danae Delbeke
Begeleider: Yanlu Li

Masterproef ingediend tot het behalen van de academische graad van
Master in de ingenieurswetenschappen: fotonica

Vakgroep Informatietechnologie
Voorzitter: prof. dr. ir. Daniël De Zutter
Faculteit Ingenieurswetenschappen
Academiejaar 2009-2010

UNIVERSITEIT
GENT

Acknowledgements

I would like to acknowledge everybody who helped me during this master thesis. First of all, I would like to thank my supervisors, Yanlu Li, prof. Roel Baets and Danae Delbeke, who guide me through this whole thesis. Many thanks go to Gunay Yurtsever of whom I could use some vital equipment for my set-up. I am also grateful to Jeroen Allaert, who filled up some gaps in my knowledge about electronics. Without him, the electronics I produced during my thesis would not work as well. Also thanks go to prof. Marc Moeneclaey who aided me in the digital frequency demodulation process.

I would also like to express my gratitude to the research people from *Cochlear*. They provided me with crucial information about the dynamics in the ear and how they are usually measured. Also, many thanks go to prof. Joris Dirckx. He shared his knowledge about laser Doppler vibrometry with me, so I could start quickly with a solid background on the subject.

Finally, I would like to address all other master thesis students from the Photonics Group. The atmosphere in the thesis student room was great and unforgettable, making it a joy to arrive early at the office and leave late.

Stijn Meersman, mei 2010

Permission to loan

"The author gives permission to make this master dissertation available for consultation and to copy parts of this master dissertation for personal use.
In the case of any other use, the limitations of the copyright have to be respected, in particular with regard to the obligation to state expressly the source when quoting results from this master dissertation."

Toelating tot bruikleen

"De auteur geeft de toelating deze masterproef voor consultatie beschikbaar te stellen en delen van de masterproef te kopiëren voor persoonlijk gebruik.
Elk ander gebruik valt onder de beperkingen van het auteursrecht, in het bijzonder met betrekking tot de verplichting de bron uitdrukkelijk te vermelden bij het aanhalen van resultaten uit deze masterproef."

Stijn Meersman, mei 2010

Analysis and Proof-of-principle Implementation of a Laser Doppler Vibrometry based Middle Ear Microphone

by

Stijn MEERSMAN

Master Thesis presented to achieve the academic degree of
Master in de ingenieurswetenschappen: fotonica

Academic year 2009–2010

Promotors: prof. dr. ir. Roel BAETS, dr. ir. Danae DELBEKE
Supervisor: ir. Yanlu LI

Faculteit Ingenieurswetenschappen
Vakgroep Informatietechnologie
Universiteit Gent

Summary

In this work the potential of photonic integration technologies for laser Doppler based hearing implants is explored. We start from theoretical considerations to find the appropriate system: heterodyne detection, which needs an optical frequency shifter. Also, a fundamental detection limit is derived. Next, we translate the general heterodyne idea to an integrated version on silicon on insulator. To realize the frequency shift, serrodyne modulation by a phase modulator is proposed. The imperfections for this method of shifting are investigated, together with their resulting effects on the performance of the optical vibrometer. Finally, we build a macroscopic fiber analogue of the suggested integrated version. Measurements are conducted on a vibrating retroreflective film and a vibrating paper, and compared with a commercial vibrometer. We were able to measure speeds on the order of 100μm/s with 200nW optical power on the detector. The main source of noise, limiting performance, is tracked down.

Keywords

laser Doppler vibrometer, serrodyne frequency shifting, ear microphone

Analysis and Proof-of-principle Implementation of a Laser Doppler Vibrometry based Middle Ear Microphone

Stijn Meersman

Supervisor(s): Yanlu Li, Roel Baets, Danae Delbeke

Abstract— **This article explores the potential of photonic integration technologies for laser Doppler vibrometer (LDV) based hearing implants. First, a fundamental limit for LDVs based on shot noise is derived and compared with the requirements for the hearing implant. Next, a possible outlook for an integrated heterodyne LDV on silicon on insulator is presented, and the use of a serrodyne frequency shifter (SFS) is proposed. The influence of a non-ideal SFS on the performance of the LDV is studied. Finally, a macroscopic version of the proposed miniature LDV is built in fiber as a proof-of-principle implementation of the integrated LDV. The SFS is found to work well. The noise equivalent speed measured was 100μm/s for a power of 200nW on the detector of the LDV. This was limited due to noise on the current driving the laser.**

Keywords— **laser Doppler vibrometer, serrodyne frequency shifting, ear microphone**

I. Introduction

LASER Doppler vibrometers (LDVs) are non-contact optical sensors for sensing vibrations of surfaces, based on the Doppler effect. They are used in a wide variety of applications ([1], [2], [3]). One of them includes ear dynamics characterization (e.g. [4]). The idea rose to develop a miniaturized LDV and to implant it in the middle ear of a hearing impaired person for measuring the sound invoked motions there. The output of the LDV can thereafter stimulate cochlear nerves via an electrical probe to provide hearing sense. The goal of this article is to discuss the feasibility of this idea and how the integrated LDV should look like. A macroscopic version is built as proof-of-principle.

II. Heterodyne LDV and fundamental limit

When a laser is shone on a moving surface, the frequency of the back reflected light will be shifted by an amount $f_D(t)$ due to the Doppler effect:

$$f_D(t) = 2\frac{v(t)}{\lambda}, \tag{1}$$

with $v(t)$ the speed parallel with the laser beam. The Doppler shift $f_D(t)$ can be recovered by interferometric methods. Heterodyne detection involves the least noise: an optical frequency shifter (OFS) in one of the arms of the interferometer can translate the signal to a low noise region in the frequency spectrum. The photocurrent $I(t)$ is

$$I(t) = R\left[P_m + P_r + 2\sqrt{P_m P_r}\cos\left(2\pi f_{FS} t + \varphi(t)\right)\right], \tag{2}$$

with P_m and P_r the optical power in the measurement and reference arm respectively, R the responsivity of the photodiode and f_{FS} the optical frequency shift. The Doppler shift is contained in $\varphi(t)$. If we assume a harmonic displacement of the surface

$$x(t) = \Delta x \cos\left(2\pi f_{vib} t\right), \tag{3}$$

with f_{vib} the vibration frequency, then the spectrum of the photocurrent will consist of frequency components at $f_{FS} \pm f_{vib}$ with magnitude $4\pi\Delta x/\lambda$, as long as $\Delta x < \lambda$.

In best case, noise is dominated by shot noise, which is inevitably present at the conversion from an optical signal to an electrical signal [5]. The shot noise in the photocurrent I_{sh} is (RMS)

$$I_{sh} = \sqrt{2qR\left(P_m + P_r\right)B}, \tag{4}$$

with q the elementary charge and B the bandwidth in which is measured. All vibration information will be lost when the frequency components at $f_{FS} \pm f_{vib}$ are buried under noise. Assuming equal magnitudes of noise and side peaks at $f_{FS} \pm f_{vib}$ for the detection limit Δx_{min} gives

$$\Delta x_{min} = \sqrt{\frac{qB\left(P_m + P_r\right)}{4\pi R P_m P_r}}\lambda. \tag{5}$$

Requirements for the optical middle ear microphone dictates that it should be able to measure displacements down to 0.1pm and vibration frequencies between 300Hz and 6kHz. At least 100mW of light power on the detector is then needed. This is 100 times above the targeted power budget of hearing implants.

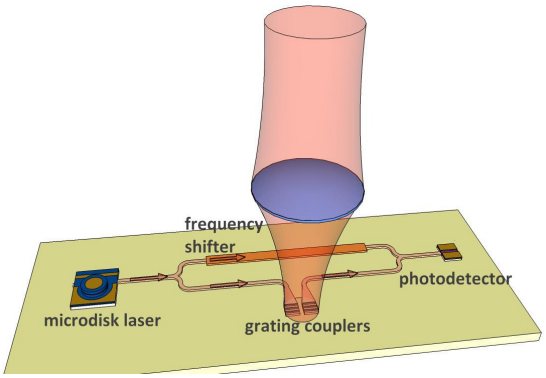

Fig. 1. Schematic outlook of an integrated LDV on SOI

III. LDV on SOI

A heterodyne LDV on SOI can look like as in Fig. 1. Laser light is split into a frequency shifting arm and a measurement arm. Light from the measurement arm can leave the photonics

S. Meersman is with the Photonics research group, Ghent University (UGent), Gent, Belgium. E-mail: Stijn.Meersman@UGent.be .

chip through a grating coupler and be focused at the vibrating object. Another grating coupler can collect the reflected light back. Light from both arms is combined and falls on a photodetector.

Laser and detector can be integrated by bonding technologies [6]. However, OFSs are not readily available on SOI. We therefore propose to use serrodyne frequency shifting (SFS). SFS is accomplished by applying a sawtooth phase modulation to the optical signal. The sawtooth should change from 0 to 2π linearly and should have an infinitely short fall time. Because there is no difference between a phase of 0 and 2π, the light sees an ever linearly increasing phase, which corresponds with a constant frequency shift. Due to the periodic nature of the sawtooth phase modulation, a non ideal sawtooth will cause a conversion of the optical signal into spurious sidebands at integer multiples of the desired frequency shift f_{FS} with respect to the original frequency. The sideband at $-f_{FS}$ will result in an error factor in the measurement, because it causes an anti-modulation of the carrier frequency f_{FS}, and should be kept as low as possible

IV. Fiber based serrodyne LDV

We have built a macroscopic version of the proposed integrated LDV with optical telecommunication components; the frequency demodulation is executed digitally. The SFS is realized with a $LiNbO_3$ phase modulator. The SFS was first evaluated and the side mode suppression between frequency components f_{FS} and $-f_{FS}$ was estimated to be lower than 33dB for f_{FS}=10kHz, corresponding with a modulation factor error smaller than 95%.

Next, vibration measurements were conducted on a retroreflective film glued to a loudspeaker. The light was pointed at the film with a focuser with an NA of 0.1. The focuser also caught the back reflected light (-20dB of the incoming signal). A circulator is inserted to separate both light beams. Careful noise analysis showed that relative intensity noise (RIN) caused by noise on the current driving the laser predominates over other noise sources. Since for RIN the signal-to-noise ratio (SNR) can be written as

$$\text{SNR} \propto \frac{\sqrt{P_m P_r}}{P_m + P_r}. \tag{6}$$

The 50:50 splitter after the laser was replaced by a 99:1 splitter in order to have more equal power in both arms and thus to improve SNR. The highest SNR we obtained for the lowest power on the detector was 40dB for a spectral bandwidth of 1Hz and a power of 200nW on the detector (equal power from both arms). This corresponds with 50μW of laser input power to the LDV. This resulted in a noise equivalent speed of 100μm/s and this is 15dB larger than when only shot noise would be present.

We applied different single frequency vibration to the loudspeaker and compared our measurements with those obtained by a commercial LDV from *Polytec*. The shape of both measurements match well, but an amplitude error was observed. The commercial LDV measured speeds with a factor 0.76 lower than our LDV. Nevertheless, we took this factor into account as a calibration factor in the following measurements and we compared both signals. We defined a figure of resemblance (FOR) as

$$\text{FOR} = 1 - \frac{\text{RMS}\left(v_P - v_f\right)}{\text{RMS}\left(v_P\right)}, \tag{7}$$

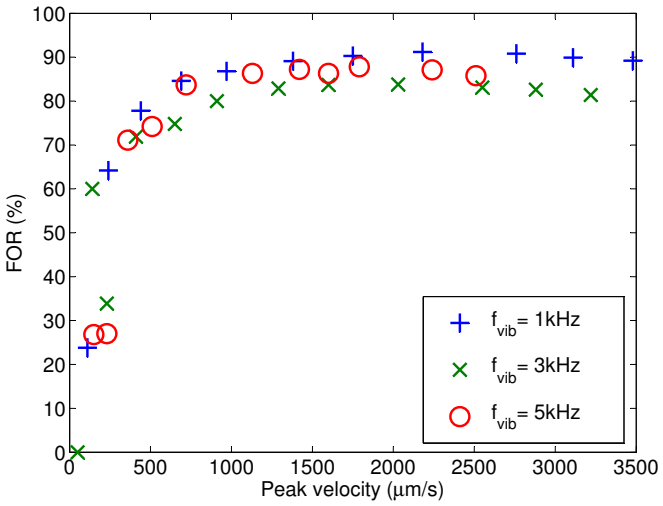

Fig. 2. FOR for different vibrating frequencies and speeds.

with v_P and v_f the vibration speed measured with Polytec's LDV and our fiber based LDV respectively. The calculated FOR for different vibration frequencies and speed are shown in Fig. 2. The trend for all vibration frequencies are the same. At speeds close to the noise equivalent speed the FOR is low. For a speed of 300μm/s the FOR is higher than 60%, and for speeds higher than 800μm/s the FOR exceeds 80%. At even higher speeds the FOR saturates and even drops slightly. This is because the bandwidth of our signal becomes larger than the bandwidth (12kHz) around f_{FS}. Information will then be lost when filtering, resulting in distortions and lower measured speed.

V. Conclusions

We derived that even in shot noise limited operation the light power on the detector, needed to measure the required displacements in the middle ear, is already 100 times the targeted power budget of a hearing implant. This limits the feasibility of an integrated LDV as middle ear microphone. Nevertheless, we built a macroscopic fiber version of a possible integrated LDV on SOI. SFS is used as frequency shifting technique. The technique was proved to work efficiently. Our fiber LDV had a noise equivalent speed of 100μm/s for a power of 200nW on the detector. This limit is imposed due to noise on the current driving the laser. Improvements can be expected when this noise is minimized.

References

[1] P. Gren, K. Tatar, J. Granstrom, N.E. Molin, and E.V. Jansson. Laser vibrometry measurements of vibration and sound fields of a bowed violin. *Measurement Science & Technology*, 17(4):635–644, Apr 2006.

[2] S. Weissner and F.E. Talke. Load/unload measurements using laser doppler vibrometry and acoustic emission. *Triboloby Internation*, 33(5-6):367–372, May-Jun 2000.

[3] N. Xiang and J. M. Sabatier. An experimental study on antipersonnel landmine detection using acoustic-to-seismic coupling. *The Journal of the Acoustical Society of America*, 113(3):1333–1341, 2003.

[4] R.L. Goode, G. Ball, S. Nishihara, and K. Nakamura. Laser Doppler vibrometer (LDV) - A new clinical tool for the otologist. *American Journal of Otology*, 17(6):813–822, Nov 1996.

[5] G. P. Agrawal. *Fiber-optic Communication Systems*. Wiley-Interscience, third edition, 2002.

[6] G. Roelkens, L. Liu, J. Brouckaert, J. Van Campenhout, F. Van Laere, D. Van Thourhout, and R. Baets. Wafer bonding and heterogeneous integration: III -V/silicon photonics. In *14th European Conference on Integrated Optics and Technical Exhibition. Contributed and Invited Papers*, pages 87–90, 2008.

Nederlandstalige samenvatting

1 Inleiding

Laser Doppler vibrometrie is een contactloze optische meetmethode om trillingen van oppervlakken te meten, gebaseerd op het Doppler effect. Laser Doppler vibrometers (LDVs) worden op verschillende terreinen gebruikt. Enkele daarvan zijn: acoustica om muziekinstrumenten en luidsprekers te karakteriseren, landmijndetectie om landmijnen op te sporen en Micro-Electro-Mechanical Systems (MEMS) om het dynamisch gedrag ervan te bepalen.

LDVs worden ook gebruikt in biologie voor het bestuderen van de dynamica in het oor. *Cochlear* is een bedrijf gespecialiseerd in cochleaire implantaten voor slechthorenden. Onderzoekers in dit bedrijf gebruiken commercieel verkrijgbare LDVs om een beter inzicht te krijgen in het menselijk gehoor. Het idee ontstond om de commerciële LDV te miniaturiseren en in het middenoor van een slechthorende te implanteren, waar het geluidstrillingen van de aanwezige structuren meet. De uitgang van de LDV kan dan gebruikt worden om gehoorszenuwen prikkelen, zodat de patiënt terug kan horen.

Het idee achter deze thesis is het potentieel van nanofotonica technologie te onderzoeken om een LDV gebaseerd hoorapparaat te ontwikkelen. Het doel van deze master thesis op zich is niet de geminiaturiseerde LDV te maken, maar eerder een proefopstelling te bouwen met daarbij een analyse van de verschillende parameters die de prestaties van het systeem beïnvloeden.

2 Theoretisch overzicht van LDVs

2.1 Laser Doppler verschuiving

Licht dat op een bewegend voorwerp wordt gereflecteerd zal een faseverschuiving ondervinden volgens,

$$\varphi(t) = \frac{4\pi}{\lambda} x_{//}(t), \tag{1}$$

met λ de golflengte van het licht en $x_{//}(t)$ de tijdsvariërende positie van het object parallel met de richting van het licht. De frequentieverschuiving f_D die hier mee overeenkomt is

$$f_D(t) = \frac{1}{2\pi}\frac{d\varphi(t)}{dt} = 2\frac{v_{//}(t)}{\lambda}. \tag{2}$$

Dit is de Doppler verschuiving.

2.2 Homodyne en heterodyne detectietechnieken

Om de Doppler verschuiving te detecteren wordt interferentie gebruikt. Er zijn twee mogelijkheden: homodyne en heterodyne detectie. Een homodyne interferometer is een gewone interferometer; in een heterodyne interferometer is er een optische frequentieverschuiver in een van de armen aanwezig. Het belangrijkste voordeel van heterodyne detectie is dat het signaal kan verschoven worden naar een frequentieband met weinig ruis. Zo kan in vergelijking met homodyne detectie 1/f ruis vermeden worden. De stroom $I(t)$ gegenereerd aan de fotodetector in een heterodyne detector kan geschreven worden als

$$I(t) = I_m + I_r + 2\sqrt{I_m I_r}\cos\left(2\pi f_{FS} t + \varphi(t)\right), \tag{3}$$

met I_m en I_r afkomstig van het licht in meetarm en referentiearm van de interferometer, f_{FS} de frequentieverschuiving en $\varphi(t)$ als in (1). Veronderstel dat het oppervlak harmonisch beweegt: $x_{//}(t) = \Delta x \cos(2\pi f_{FS} t)$ (f_{vib} is de vibratiefrequentie). Voor $\Delta x < \lambda$ zal het spectrum van de fotodetectorstroom bestaan uit componenten f_{FS} en $f_{FS} \pm f_{vib}$.

2.3 Fundamentele detectielimiet

Verschillende ruisbronnen kunnen aanwezig zijn in een LDV: relatieve intensiteitsruis, thermische en versterkingsruis in de electronica na de fotodetector,... Hagelruis is echter onvermijdelijk, omdat het een quantumverschijnsel is. Met dit in het achterhoofd kan een kleinste verplaatsing Δx_{min} gemeten worden volgens

$$\Delta x_{min} = \sqrt{\frac{qB\,(P_m + P_r)}{4\pi R P_m P_r}}\lambda, \tag{4}$$

met P_m en P_r het lichtvermogen in respectievelijk de meetarm en refererentiearm van de LDV, q de elementaire eenheidslading en B de bandbreedte waarin gemeten wordt. Deze zal als uitersten $f_{FS} \pm f_{max,vib}$ moeten omvatten, met $f_{max,vib}$ de hoogste vibratiefrequentie die we wensen te meten. Voor een oormicrofoon is $f_{max,vib}$=6kHz en dus B=12kHz. De kleinste verplaatsingen die een oormicrofoon moet meten zijn in de orde van 0.1pm. Het minimale vermogen dat nodig is om dit te bereiken is volgens (4) 100mW ($=P_{tot} = 2P_m = 2P_r$). Dit is in tegenstrijd met het gelimiteerde vermogen van de batterijen waarop een hoorimplantaat moet werken.

3 Naar een geïntegreerde LDV op SOI

3.1 Uitzicht van een geïntegreerde LDV op SOI

Het uiteindelijk doel is om een geïntegreerde LDV op SOI te ontwikkelen. Die zou er kunnen uitzien als in Fig. 1. Laser en detector kunnen geïntegreerd worden met behulp van bonding technologie [1]. Een optische frequentieverschuiver is echter niet direct beschikbaar.

3.2 Serrodyne frequentieverschuiving

Om toch een frequentieverschuiving te realiseren, kunnen we gebruik maken van serrodyne modulatie. Een fasemodulator verandert de fase van het licht lineair van 0 naar 2π en dan ogenblikkelijk terug naar 0. Dit gebeurt in een periodieke manier zodat er een

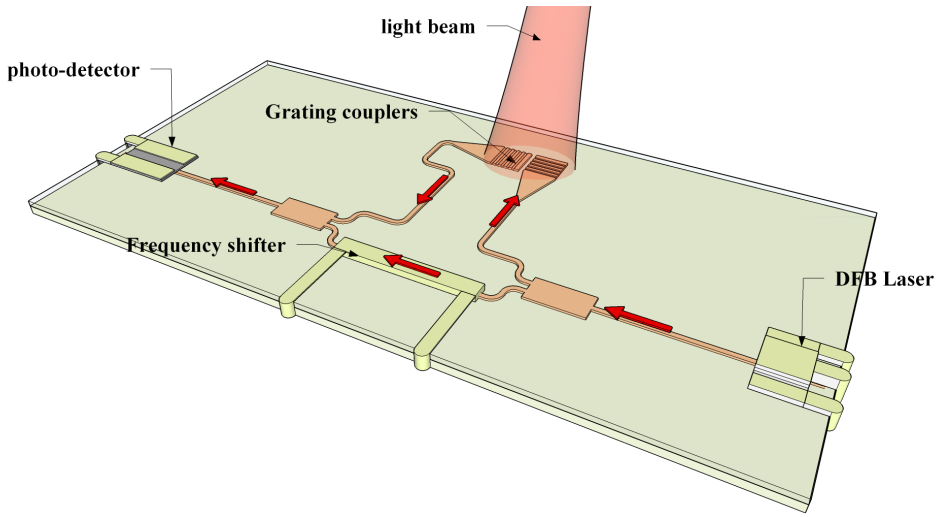

Figuur 1: Voorstelling van een geïntegreerde LDV.

zaagtandmodulatie ontstaat. Aangezien er geen verschil is tussen 0 en 2π, ziet het licht een lineair stijgende fase volgens

$$\phi(t) = 2\pi \frac{t}{T}, \tag{5}$$

met T de periode van de zaagtand. Dit resulteert in een constante frequentievershuiving

$$f_{FS} = \frac{1}{2\pi} \frac{d\phi(t)}{dt} = \frac{1}{T}. \tag{6}$$

Verschillende afwijkingen van de ideale zaagtand kunnen zich voordoen, zoals een niet oneindige korte terugvaltijd, niet-lineariteit in de helling en het overstijgen van 2π. De modulatie zal nog steeds periodiek blijven, maar andere frequentiecomponenten $f_0 + nf_{FS} (n \in \mathbb{Z})$ zullen ontstaan. Deze kunnen weggefilterd worden behalve de component met frequentie $f_0 - f_{FS}$. Deze frequentiecomponent zal aanleiding geven tot een anti-modulatie van $\varphi(t)$ in (3) en de gemeten modulatie $\psi(t)$ zal verschillen met $\varphi(t)$ volgens

$$\psi(t) \approx \left(1 - 2\frac{E_{-1}}{E_1}\right) \varphi(t), \tag{7}$$

met E_{-1}/E_1 de verhouding van de elektrische velden met frequentie $f_0 - f_{FS}$ en $f_0 + f_{FS}$. Deze formule geldt enkel voor kleine waarden van E_{-1}/E_1, voor grotere waarden zullen er distorsies optreden. De frequentiecomponent $f_0 - f_{FS}$ moet dus zo klein mogelijk gehouden worden om een correcte meting te kunnen uitvoeren.

4 Realisatie van een glasvezel gebaseerde LDV

4.1 De opstelling

Een macroscopische versie van het geïntegreerde voorstel in Fig. 1 werd gebouwd in glasvezel met behulp van optische telecommunicatiecomponenten. Een DFB laser met λ=1550nm en een InGaAs fotodiode werden gebruikt als bron respectievelijk detector. Om de serrodyne frequentieverschuiving te realiseren maakten we gebruik van een elektro-optische $LiNbO_3$ fasemodulator, aangedreven door een signaalgenerator die de gewenste zaagtand aanlegde. De uitgangsstroom van de fotodiode werd omgezet tot een spanning met een eigen gemaakte transimpedantie versterker. Deze kon dan verbonden worden met de geluidskaart van een computer. Met behulp van digitale signaalverwerking werd de eigenlijke vibratie teruggevonden. De bandbreedte die gebruikt werd was 12kHz, tweemaal de maximale vibratiefrequentie die we wensen te meten.

4.2 Evaluatie van serrodyne frequentieverschuiving

Eerst evalueerden we de serrodyne frequentieverschuiving. De spanning werd zaagtandsgewijs verandert tussen $-V_\pi$ en V_π, de negatieve en positieve spanning om een faseverandering van π te verkrijgen. We zochten naar een optimale waarde voor V_π door naar de zijbanden in het spectrum te kijken (f_{FS}=10kHz). Dit is weergegeven in Fig. 2(a). Een optimale waarde is V_π=3.54V. Met (7) werd er geschat dat deze optimale waarde overeenstemt met een fout kleiner dan 5% in de modulatie. Een detail van de niet gedemoduleerde output van de LDV voor deze optimale waarde is voorgesteld in Fig. 2(b)

We zien dat in Fig. 2(a) de zijband onderdrukking niet monotoon daalt naar het minimum rond V_π=3.54V. Dit komt door de polarisatiegevoeligheid van de fasemodulator. Kleine afwijkingen van de ideale polarisatie invoer zijn de grootste oorzaak voor de zijbanden.

Een uitgevoerde ruisanalyse toonde aan dat de grootste ruiscomponent afkomstig is

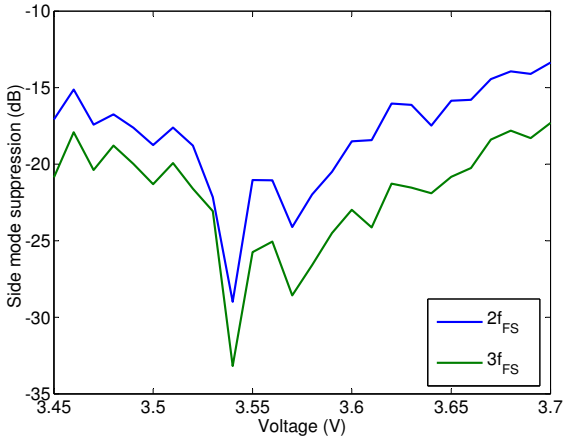

(a) Zijband onderdrukking in dB ($=P_{nf_{FS}}/P_{f_{FS}}$) in functie van spanning V_π.

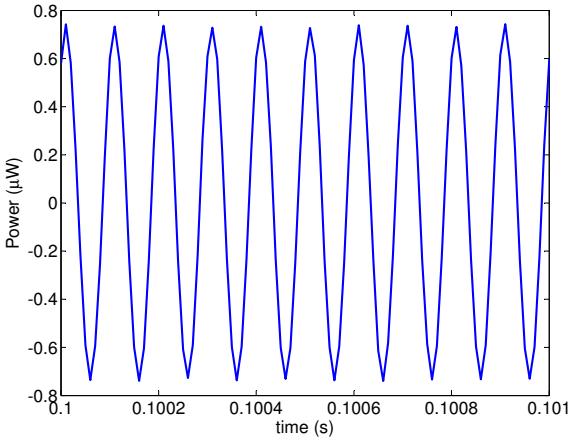

(b) Detail van LDV output (niet gedemoduleerd) voor V_π=3.54V. Sampling frequency is 100kHz.

Figuur 2: De optimale waarde voor V_π, f_{FS}=10kHz.

van ruis op de stroom die de laser aanstuurt. De SNR per spectrale bandbreedte van 1Hz, hierna kort genoteerd als SNR*, is hierdoor gelimiteerd tot 40dB. Verhoging van de SNR kan gerealiseerd worden door een betere aanstuurbron te gebruiken of gebalanceerde detectie (zie [2] voor meer informatie).

4.3 Vibratiemetingen

Hier worden de uitgevoerde vibratiemetingen besproken. Eerst wordt er een kleine aanpassing aan de opstelling uitgevoerd, nu we weten waar de grootste ruiscomponent vandaan komt. Daarna voeren we metingen uit op een retroreflectieve film en een stukje papier die op een luidspreker geplakt zijn.

4.3.1 Gelimiteerde SNR

Een focuser met numeriek apertuur van 0.1 is gebruikt om het licht van de fiber te focuseren op het bewegende oppervlak. Deze focuser vangt ook het gereflecteerde licht terug op. Een circulator is gebruikt om het inkomende licht te scheiden van het gereflecteerde. Het verlies aan optisch vermogen door de beperkte apertuur is 20dB aan de retroreflectieve film.

De ruis veroorzaakt door de ruis op de aanstuurstroom van de laser leidt tot een SNR in de vorm van

$$\text{SNR} \propto \frac{\sqrt{P_m P_r}}{P_m + P_r}. \tag{8}$$

Om de SNR te optimaliseren werd de 50:50 splitter na de laser vervangen door een 99:1 splitter (overeenkomstig het verlies aan de focuser), zodat in beide armen van de LDV gelijke lichtvermogens aanwezig zijn. Merk op dat het verhogen van het vermogen de SNR niet doet veranderen. Dit geldt ook voor het verlagen ervan. We verlagen het optisch vermogen dus totdat een andere ruiscomponent ook belangrijk wordt. Dit blijkt de ruis afkomstig van de geluidskaart te zijn.

We kunnen zo het vermogen op de detector verlagen tot 200nW, wat overeenstemt met ongeveer 50μW invoer van laserlicht in de LDV. De SNR* is dan gelijk aan 40dB, waarmee een ruis equivalente snelheid van 100μm/s overeenstemt (dit is de snelheid gemeten wanneer geen vibratie is aangelegd). Hiervoor worden wel omgevingstrillingen, die frequentie lager dan 300Hz hebben, uitgefilterd.

4.3.2 Vibratiemetingen op een retroreflectieve film

We voerden metingen uit met de beschreven opstelling en vergeleken deze met metingen uitgevoerd met een commerciële LDV van *Polytec*. Een voorbeeld van deze vergelijking voor een vibratie met snelheid voldoende boven de ruis equivalente snelheid is weergegeven in Fig. 3. De gelijkenis in vorm is duidelijk zichtbaar, maar er is een amplitudefout. De exacte reden van deze amplitudefout is niet bekend, maar kan mogelijk gerelateerd zijn met het feit dat de LDVs op verscheidene afstanden gepositioneerd zijn. In verdere metingen wordt deze fout behandelt als een calibratiefout waarmee al onze metingen worden gecorrigeerd.

We vergelijken beide metingen door een gelijkeniscijfer (FOR) te berekenen:

$$\text{FOR} = 1 - \frac{\text{RMS}\,(v_P - v_f)}{\text{RMS}\,(v_P)}, \tag{9}$$

v_P is de snelheid gemeten met de LDV van Polytec, v_f de snelheid gemeten met onze glasvezelopstelling. Ideaal is er complete gelijkenis en is de FOR gelijk aan 100%. Het

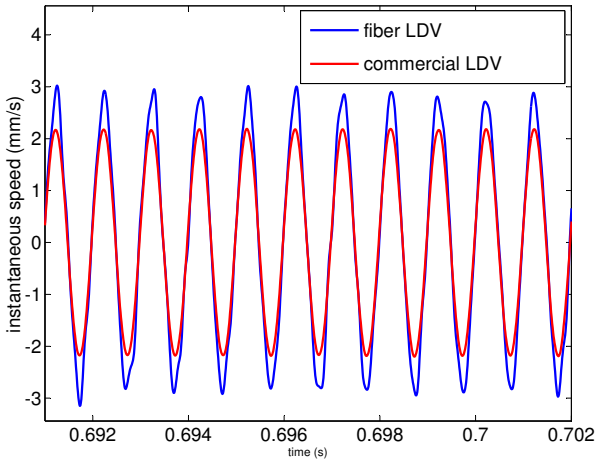

Figuur 3: Vergelijking tussen de commerciële en glasvezel LDV.

resultaat hiervan is weergegeven in Fig. 4. De FOR is onafhankelijk van de vibratiefrequentie en overstijgt 60% voor een snelheid die gelijk is aan driemaal de ruis equivalente snelheid (=300μm/s). Een FOR hoger dan 80% wordt bereikt voor tienmaal de ruis equivalente snelheid (=1000μm/s). Voor hogere snelheden satureert de FOR en neemt zelfs lichtjes af. Dit komt doordat de bandbreedte van het signaal groter wordt dan de bandbreedte waarmee we werken. We kunnen deze laten toenemen, maar dan zal ook de ruis equivalent snelheid toenemen.

4.3.3 Vibratiemetingen op een papier

We voerden ook vibratiemetingen uit op een stukje gerecycleerd papier. Dit om het effect na te bootsen van extra verliezen die we kunnen verwachten, wanneer een LDV wordt gericht op een structuur in het middenoor. We gebruikten dezelfde opstelling als hiervoor, met eenzelfde ingangsvermogen (50μW). Het verlies aan de focuser nam van 20dB toe naar 33dB. Het vermogen dat aankomt is nu niet meer 200nW, maar 105nW. We werken nog net in het gebuid waar de ruis van de sturingstroom van de laser groter is dan die van de geluidskaart. Maar doordat het optisch vermogen niet meer gelijk is verdeeld in beide armen (P_m=5nW en P_r=100nW) zakt de SNR met 4dB (zie (8)). Dit correspondeert met een ruis equivalent snelheid die 4dB hoger is, wat ook werd opgemeten. Resultaten voor de FOR zijn weergegeven in Fig. 5 (enkel 1 vibratiefrequentie weergegeven, andere

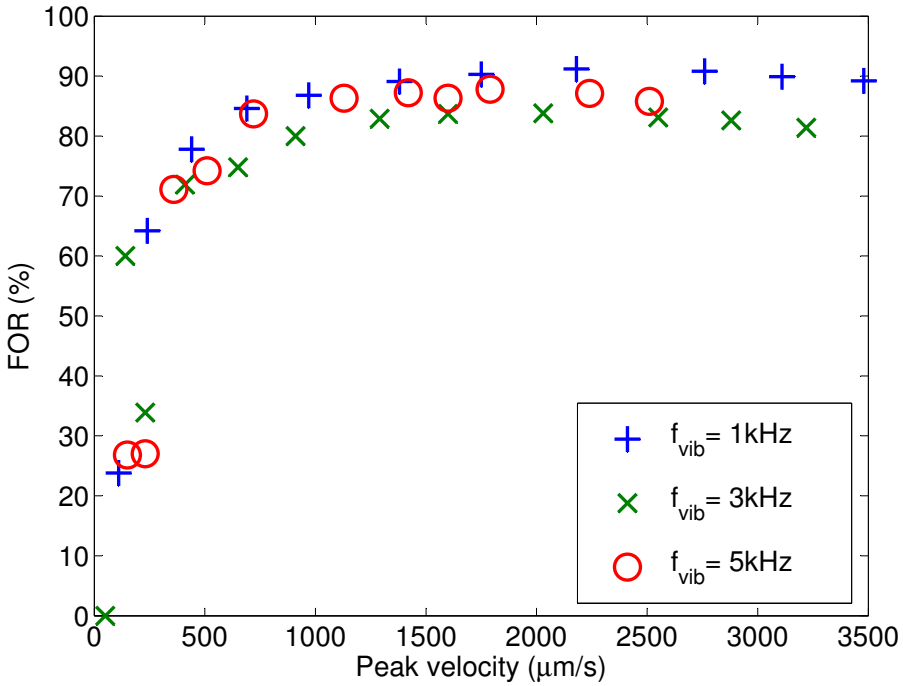

Figuur 4: FOR voor verschillende vibratiefrequenties en snelheden.

frequenties zijn gelijkaardig). Voor eenzelfde FOR moet nu inderdaad een hogere snelheid aangelegd worden.

5 Conclusies

Een glasvezel LDV werd gebouwd als macroscopische versie van een mogelijke geïntegreerde LDV. De frequentieverschuiver werd gerealiseerd met behulp van serrodyne frequentieverschuiving. De serrodyne techniek werd geevalueerd en de lage zijbanden die werden teruggevonden, zouden een fout kleiner dan 5% veroorzaken op de meting. Eerst werden metingen op een vibrerende retroreflectieve film uitgevoerd. De hoogste SNR* die we konden bereiken met het laagste optische vermogen was 40dB met 200nW op de detector of 50μW invoer vermogen van de laser. De ruis was afkomstig van de ruis op de aanstuurstroom van de laser. Een ruis equivalente snelheid van 100μm/s werd opgemeten. Vergelijking met een commercieel apparaat toonde dat de vorm van beiden overeenstemden, maar dat er een amplitudefout optrad. Deze fout werd in rekening gebracht bij de

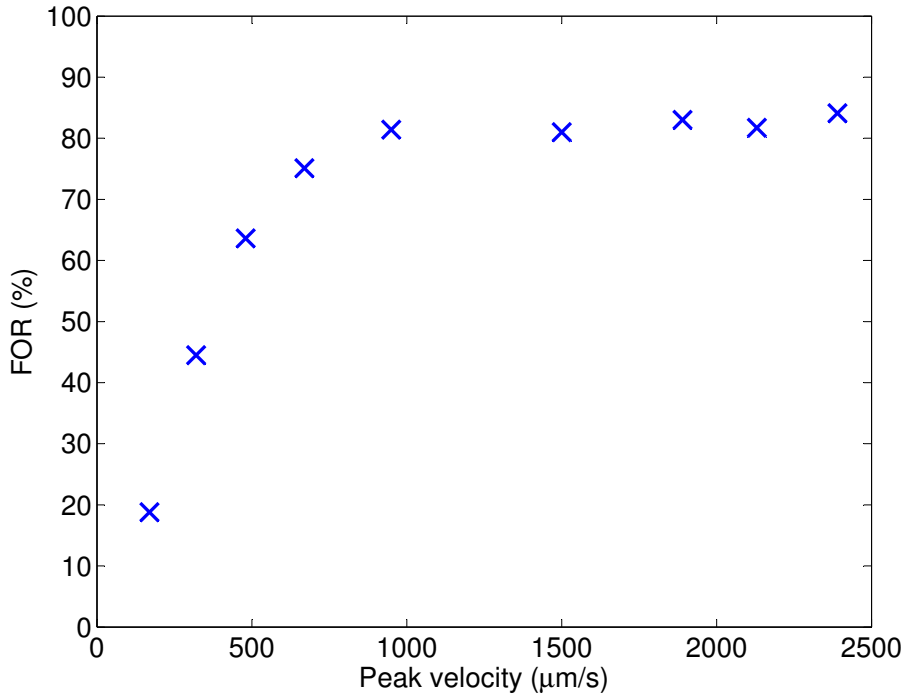

Figuur 5: FOR in functie van snelheid voor vibrerend stuk papier f_{vib}=3kHz

rest van de metingen. Uiteindelijk voerde we ook metingen uit op een stukje papier. Het extra verlies aan dit object was 13dB, wat resulteerde in een SNR verlies van 4dB en dus een ruis equivalente snelheid die 4dB hoger was.

Theoretische berekeningen toonden aan dat een optisch vermogen 100 maal groter dan het beschikbare vermogenbudget voor een oorimplantaat nodig is om de kleinste bewegingen te kunnen meten. Dit is een probleem voor de verdere ontwikkeling van de LDV gebaseerde middenoor microfoon.

Contents

List of Acronyms

ADC	Analog to Digital Converter
BW	Bandwidth
DC	Direct Current
DFB	Distributed Feedback
DOF	Depth Of Focus
FM	Frequency Modulation
FOR	Figure Of Resemblance
LDV	Laser Doppler Vibrometer
$LiNbO_3$	Lithium Niobate
MEMS	Micro-Electro-Mechanical Systems
NA	Numerical Aperture
OFS	Optical Frequency Shifter
PC	Polarization Controller
RIN	Relative Intensity Noise
RMS	Root Mean Square
RMSE	Root Mean Square Error
SAW	Surface Acoustic Wave
SNR	Signal-to-Noise Ratio
SNR^*	Signal-to-Noise Ratio for spectral bandwith of 1Hz
SFS	Serrodyne Frequency Shifter
Si	Silicon
SiO_2	Silicon Oxide

SOI	Silicon On Insulator
SPL	Sound Pressure Level
TE	Transverse Electric
TIA	Transimpedance Amplifier
TM	Transverse Magnetic

Chapter 1

Introduction

Laser Doppler vibrometry is a non-contact optical measurement method for sensing vibrations of surfaces. Laser Doppler velocimetry or anemometry is its counterpart for determining the direction and speed of fluids. They are both based on the detection of the laser Doppler shift, which is the change in frequency of light resulting from reflection on a moving object.

Nowadays Laser Doppler vibrometers (LDVs) are exploited in a wide variety of applications. In acoustics, LDVs have been used to measure the performance of musical instruments and speakers [3]. LDVs are also employed in hard disk analysis: they make it possible to analyze the head positioning in hard disk drives [4]. Next to this, LDVs are widely used to characterize the dynamic response of Micro-Electro-Mechanical Systems (MEMS) [5]. A more noble application is in the field of land mine detection. LDVs can locate land mines by distinguishing the typical ground movements, upon excitation of a specific sound wave, when a land mine is present [6].

Another important application for this work is in the field of biology: ear dynamics characterization. In 1968, Khanna and his coworkers first demonstrated an LDV-like configuration to measure submicroscopic vibrations in ears of animals [7]. Since then many effort has been spent in detecting weaker vibrations (e.g. [8]) and easier alignment procedures (e.g. [9]).

Cochlear is a company specialized in advanced hearing loss solutions offering cochlear

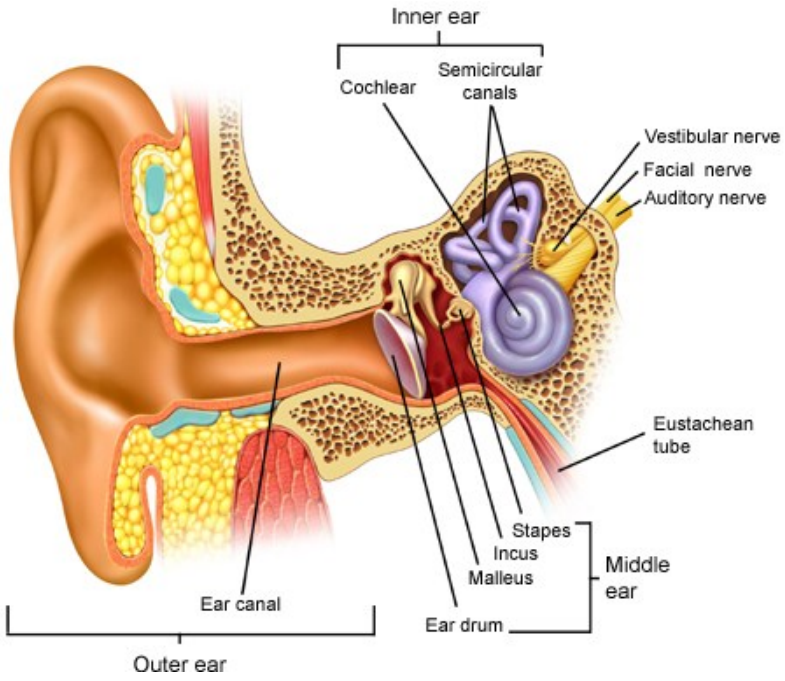

Figure 1.1: Anatomy of the ear. Virtual Medical Centre. "Anatomy of the ear." Image from "Ear-summary." `http://www.virtualmedicalcentre.com/anatomy.asp?sid=29` (May 2010)

implants for adults and children. Researchers at this company use commercially available LDVs to study dynamics in the ear. The idea rose to miniaturize the commercial LDV and to implant it in the middle ear (Fig. 1.1) of a hearing impaired person for measuring the sound invoked motions there. The output of the implanted miniaturized LDV can thereafter stimulate cochlear nerves via an electrical probe to provide hearing sense. An advantage of this idea is that one can still benefit from the intact structures in the ear, which could improve sound quality sensed by impaired people.

The middle ear microphone requires a good sensitivity for vibrations with frequencies between 300Hz and 6kHz and within the range of 25 and 90dB SPL (sound pressure level). Corresponding displacement amplitudes are given in Table 1.1. Implanted batteries limit the available power for the middle ear microphone and a total power budget of 1mW or lower should be targeted for the implanted LDV.

The context behind this master thesis is to explore the potential of photonic integration

	300Hz	1kHz	6kHz
90dB SPL	10nm	50nm	1nm
50dB SPL	100pm	500pm	10pm
25dB SPL	5pm	25pm	0.5pm

Table 1.1: Vibration amplitudes in the inner ear for different frequencies and sound pressure levels

technologies for LDV based hearing implants. The long term vision established is to develop a fully integrated LDV on silicon-on-insulator (SOI) which could be used as a middle ear microphone. The goal of this thesis is not to make a fully integrated LDV, but rather to have a proof-of-principle implementation of an LDV for submicroscopic vibrations, together with analyses of the parameters influencing the performance of the system. It should eventually lead the way to the further development of an integrated, implantable middle ear microphone.

Chapter 2

Theoretical overview of LDV

In this chapter, the reader should get confident with the theory behind LDVs. First, the laser Doppler shift is introduced. This shift is the basis behind LDVs. It is imposed by the vibrating object and contains information about the movement of the object. Then, two methods to detect this shift are discussed: homodyne and heterodyne detection. Their working principles are explained in detail, together with their merits and drawbacks. The optical frequency shifter needed for heterodyne detection is discussed, together with the demodulation process. In a last section, we take a closer look at the different possible noise sources in LDVs. We will be able to derive a fundamental limit on the performance of the LDV based on shot noise.

2.1 Laser Doppler shift

The Doppler effect is named after the physicist Christian Doppler (1803-1853) who first proposed it in 1842. The Doppler shift is the frequency change of a wave stemming from a relative movement between source and observer of the wave. The observer detects a higher frequency when the source moves towards it and a lower one when the source moves away. This is depicted in Fig. 2.1(a). We can hear this effect when an emergency vehicle with sirens passes by. Since light is also a wave, the Doppler effect also applies to it. The demonstration of a laser Doppler shift was first shown in 1964 by Yeh and Cummins [10].

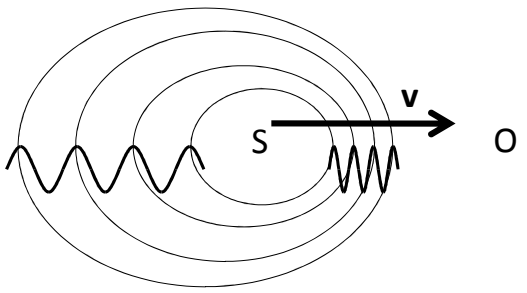

(a) S = source, O = observer, v = velocity. Wavefronts in direction of movement are closer together and an observer there will experience a higher frequency.

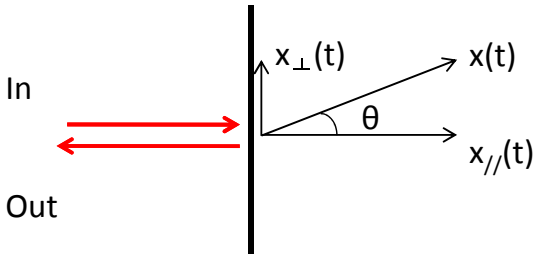

(b) In = incoming light; Out = reflected light; x(t) is time varying displacement vector; θ is the angle between the displacement x(t) and the normal of the surface.

Figure 2.1: The Doppler effect

If light is shone on a moving surface as in Fig. 2.1(b), the reflected light will have a time varying phase shift $\varphi(t)$ according to the position of the surface,

$$\varphi(t) = \frac{4\pi}{\lambda} x_{//}(t), \tag{2.1}$$

with λ the wavelength of the light and $x_{//}(t)$ the time varying position parallel to the propagation direction of the light. $x_{//}(t)$ is related to the position $x(t)$ as

$$x(t) = x_{//}(t)\cos(\theta). \tag{2.2}$$

This time varying phase gives rise to the Doppler shift f_D:

$$f_D(t) = \frac{1}{2\pi}\frac{d\varphi(t)}{dt} = 2\frac{v_{//}(t)}{\lambda}, \tag{2.3}$$

with $v_{//}$(t) the speed of the surface parallel to the propagation direction of the light.

Doppler frequency shifts for a HeNe laser and telecom laser and different speeds $v_{//}$ are shown in Table 2.1.

	HeNe laser ($\lambda = 632$nm)	Telecom laser ($\lambda = 1550$nm)
v = 1mm/s	3.2kHz	1.3kHz
v = 0.8m/s	2.5MHz	1MHz

Table 2.1: Examples of Doppler frequency shifts.

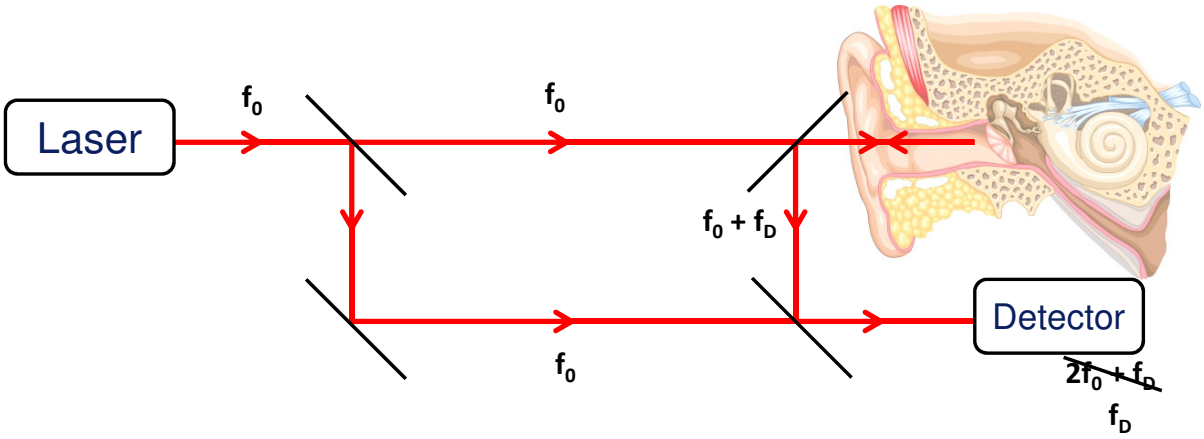

Figure 2.2: The homodyne arrangement for acquiring the Doppler shift.

2.2 Homodyne and heterodyne detection techniques

As seen in Table 2.1 the frequency shifts caused by the Doppler shifts are rather small compared to the linewidth of most lasers. Measuring the Doppler shift directly with an optical spectrum analyzer would be impossible. To detect the shift an interferometer can be used. Two different interferometric configurations are common: the homodyne and heterodyne detection techniques.

2.2.1 Homodyne detection

The homodyne arrangement is given schematically in Fig. 2.2. This is in fact just a Mach-Zehnder interferometer. The laser light with frequency f_0 is split by a half transparent mirror into a reference and measurement arm. The measurement arm goes to the vibrating object under interest and the frequency of the light is shifted due to the Doppler effect.

The electric fields in reference arm E_r and E_m can be expressed as

$$E_r(t) = E_r \cos(2\pi f_0 t), \tag{2.4}$$

$$E_m(t) = E_m \cos(2\pi f_0 t + \varphi(t) + \theta). \tag{2.5}$$

The phase θ stems from a constant path difference in the interferometer, $\varphi(t)$ is as in Eq. (2.1). Everything is combined again at the photodetector. The photodetector current is proportional to the square of the incident field leading to sum and difference frequencies, of which the former is far beyond the bandwidth of the detector. The created current at the photodetector will look like

$$I(t) = I_r + I_m + 2\sqrt{I_r I_m}\cos(\varphi(t) + \theta), \tag{2.6}$$

with I_r the current stemming from light power in the reference arm and I_m stemming from the power in the measurement arm. Since the phase $\varphi(t)$ and the Doppler shift $f_D(t)$ are interrelated according to Eq. (2.3), Eq. (2.6) can also be written as

$$I(t) = I_r + I_m + 2\sqrt{I_r I_m}\cos\left(2\pi \int_0^t f_D(\tau)\, d\tau + \theta'\right) \tag{2.7}$$

Assume that the vibration is harmonic:

$$x_{//}(t) = \Delta x \cos(2\pi f_{vib} t), \tag{2.8}$$

with Δx the displacement amplitude and f_{vib} the frequency of vibration. First, assume that θ = -π/2. Since for movements in the inner ear $\Delta x < \lambda$, Eq. (2.6) can be approximated as

$$I(t) \approx \mathrm{DC} + 2\sqrt{I_r I_m}\frac{4\pi}{\lambda}\Delta x \cos(2 f_{vib} t). \tag{2.9}$$

The output current will oscillate with the same frequency as the vibration. If θ changes to π/2, $I(t)$ becomes:

$$I(t) \approx \mathrm{DC} - 2\sqrt{I_r I_m}\frac{4\pi}{\lambda}\Delta x \cos(2 f_{vib} t). \tag{2.10}$$

Since one can not distinguish practically between θ equal to π/2 or -π/2, one does not know whether Eq. (2.9) or Eq. (2.10) applies. So, the sign of the oscillating part is not

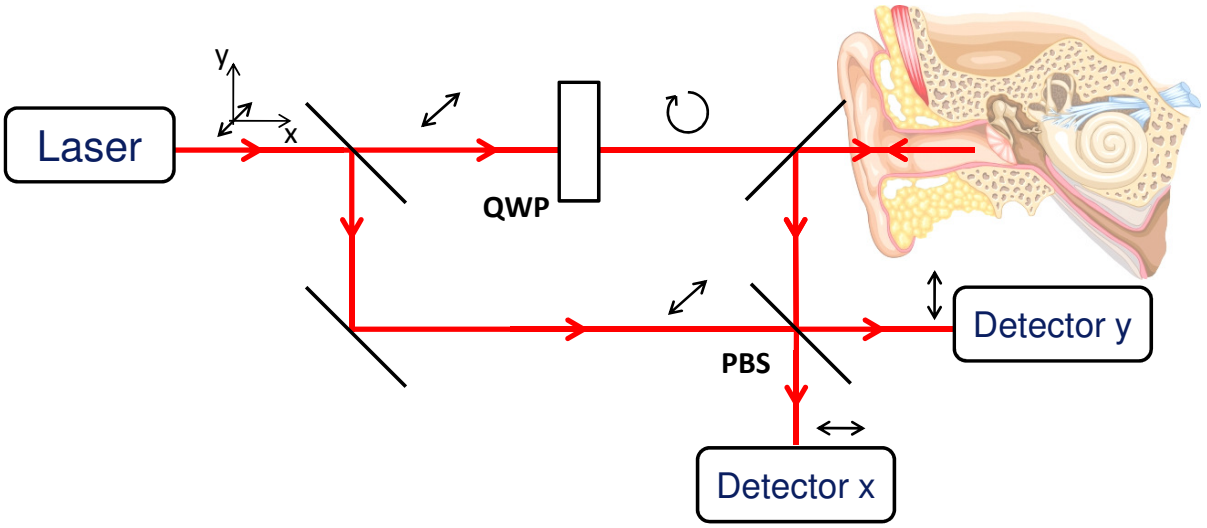

Figure 2.3: The quadrature homodyne configuration for acquiring the Doppler shift. QWP = quarter wave plate, PBS = polarizing beam splitter.

determined, which corresponds with a direction ambiguity. Using homodyne detection, one can not know whether the object is moving away or coming closer. Now, assume θ to be zero or a multiple of 2π:

$$I(t) \approx \mathrm{DC} + 2\sqrt{I_r I_m}\left[1 - \frac{4\pi^2}{\lambda^2}\Delta x^2 \cos^2\left(2\pi f_{vib} t\right)\right]. \tag{2.11}$$

The output current will not oscillate with frequency f_{vib}, but with double frequency $2f_{vib}$. In conclusion, the output is dependent on the phase θ and is only linearly related to the position if $\theta = \pm\pi/2$ and as long as $\Delta x\,(t) < \lambda$. *To make this configuration work properly, the path difference between the arms should be controlled to a fraction of the wavelength.*

2.2.2 Homodyne quadrature detection

An alternative to the previous configuration is homodyne quadrature detection: two photodetectors are used with output signals in quadrature. This can be done by polarizing optics as demonstrated in Fig. 2.3. A laser has a polarization of 45° wrt. an x and y axis and is split in a reference and measurement arm. The electric field in each arm can be

expressed as (complex notation)

$$\boldsymbol{E_r}(t) = (|E_r|\,\mathbf{1_x} + |E_r|\,\mathbf{1_y})\,e^{j2\pi f_0 t}, \tag{2.12}$$

$$\boldsymbol{E_m}(t) = (|E_m|\,\mathbf{1_x} + |E_m|\,\mathbf{1_y})\,e^{j2\pi f_0 t}, \tag{2.13}$$

with $\mathbf{1_x}$ and $\mathbf{1_y}$ unit vectors along x and y axis. Now, a quarter wave plate is placed in the measurement arm making the light circularly polarized and it then reflects on the vibrating object. The electric field in the measurement arm changes to

$$\boldsymbol{E_m}(t) = (|E_m|\,\mathbf{1_x} - j\,|E_m|\,\mathbf{1_y})\,e^{j(2\pi f_0 t + \varphi(t) + \theta)}. \tag{2.14}$$

At the end, a polarizing beam splitter sends the x-polarized components of the electric fields to one photodetector and the y-polarized components to another. The electric fields at the different photodetectors are 45° out of phase:

$$\boldsymbol{E_x}(t) = \left(|E_r| + |E_m|\,e^{j(\varphi(t)+\theta)}\right)e^{j2\pi f_0 t}\mathbf{1_x} \tag{2.15}$$

$$\boldsymbol{E_y}(t) = \left(|E_r| - j\,|E_m|\,e^{j(\varphi(t)+\theta)}\right)e^{j2\pi f_0 t}\mathbf{1_y}. \tag{2.16}$$

The photocurrent at each detector can be found by taking the real part of the electric field at each detector, square it and neglect terms with optical frequencies. The resulting currents will be in quadrature after removing the DC components:

$$I_x(t) \propto \cos(\varphi(t) + \theta) \tag{2.17}$$

$$I_y(t) \propto \sin(\varphi(t) + \theta). \tag{2.18}$$

The displacement information can be obtained by e.g. an arctan operation. No phase control is needed and the limitation that the displacement has to be smaller than the wavelength has disappeared.

Note that both homodyne techniques work around DC and inevitably suffer from 1/f noise or flicker noise, which is present in each electronic device [11]. It results from a variety of effects, such as impurities in resistors and base noise current in transistors.

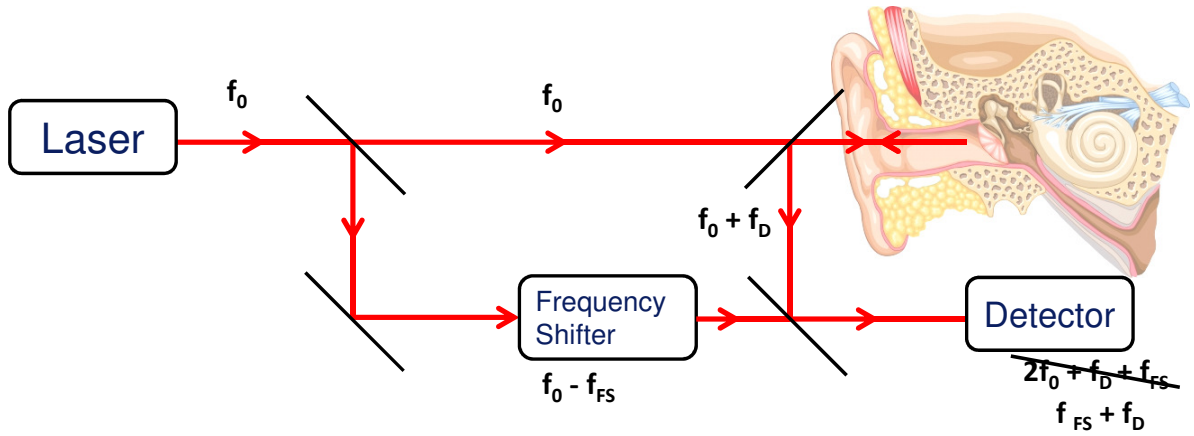

Figure 2.4: The heterodyne arrangement for acquiring the Doppler shift.

2.2.3 Heterodyne detection

The heterodyne detection technique allows circumventing 1/f noise and allows working with only one detector. The only difference between the homodyne and heterodyne detection is that an optical frequency shifter, which is able to create a time invariant frequency shift f_{FS}, is inserted in the reference arm (Fig. 2.4). The output of the detector becomes:

$$I(t) = I_r + I_m + 2\sqrt{I_r I_m}\cos\left(2\pi f_{FS} t + \varphi(t) + \theta\right). \tag{2.19}$$

This looks exactly like a frequency modulated signal with carrier frequency f_{FS}, the modulation is contained in $\varphi(t)$. Assume that the vibrating surface is moving in a harmonic way as in Eq. (2.8). The output at the detector becomes:

$$I(t) = \mathrm{DC} + 2\sqrt{I_r I_m}\cos\left(2\pi f_{FS} t + \frac{4\pi\Delta x}{\lambda}\cos\left(2\pi f_{vib} t\right) + \theta\right). \tag{2.20}$$

The frequency spectrum of the time varying part of the current can be found through Bessel functions ($\beta = 4\pi\Delta x/\lambda$):

$$\begin{aligned}
&\cos\left(2\pi f_{FS} t + \beta\cos\left(2\pi f_{vib} t\right)\right) = J_0(\beta)\cos\left(2\pi f_{FS} t\right) \\
&+ \sum_{n=1}^{\infty}(-1)^n J_{2n}(\beta)\left[\cos\left(2\pi\left(f_{FS} + 2nf_{vib}\right)t\right) + \cos\left(2\pi\left(f_{FS} - 2nf_{vib}\right)t\right)\right] \\
&- (-1)^n J_{2n+1}(\beta)\left[\cos\left(2\pi\left(f_{FS} + (2n+1)f_{vib}\right)t\right) + \cos\left(2\pi\left(f_{FS} - (2n+1)f_{vib}\right)t\right)\right]
\end{aligned} \tag{2.21}$$

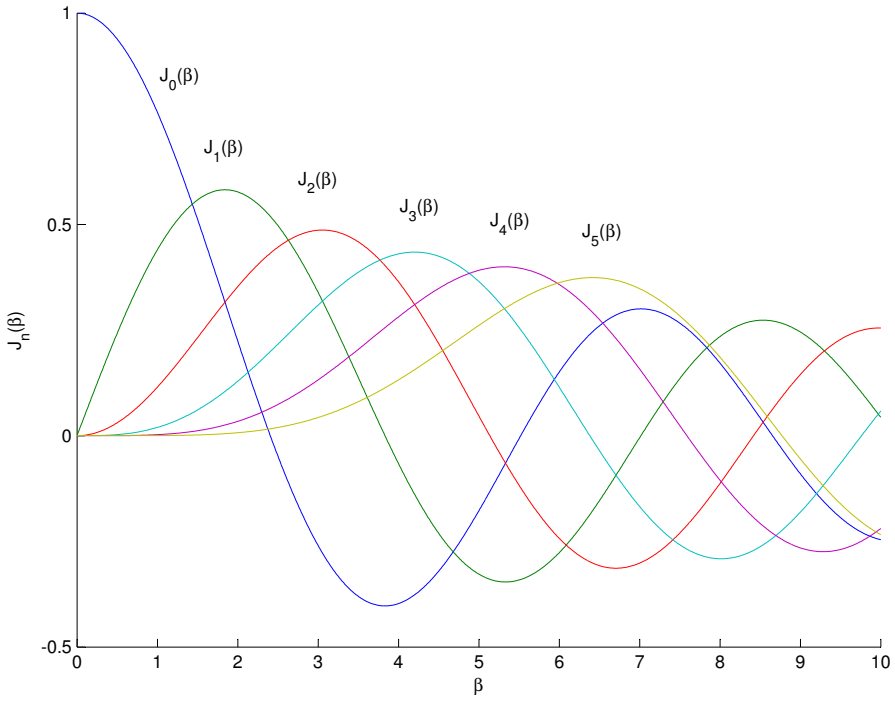

Figure 2.5: The Bessel functions, order 0 to 5.

The static phase θ is dropped, since it will not influence the actual spectrum. The spectrum consists of peaks at f_{FS} plus and minus multiples of the vibration frequency, with magnitudes dependent on $J_n(\beta)$. The Bessel functions are plotted in Fig. 2.5. For small β the spectrum will only consist of the carrier frequency with small side peaks at $f_{FS} \pm f_{vib}$, when β becomes larger more side peaks will appear. A handy rule of thumb, Carson's rule, says that most of the power (>98%) of a FM signal is contained in a bandwidth BW of

$$BW = 2\left(f_{vib} + f_D\right) \tag{2.22}$$

around the carrier frequency [12]. To reduce noise a bandpass filter centered at f_{FS} and bandwidth as in Eq. (2.22) can be placed. In this way 1/f noise can be filtered out.

2.2.4 Summary

The homodyne technique looks like the simplest one to implement. However, careful analysis showed that one needs to control the path difference in the interferometer down

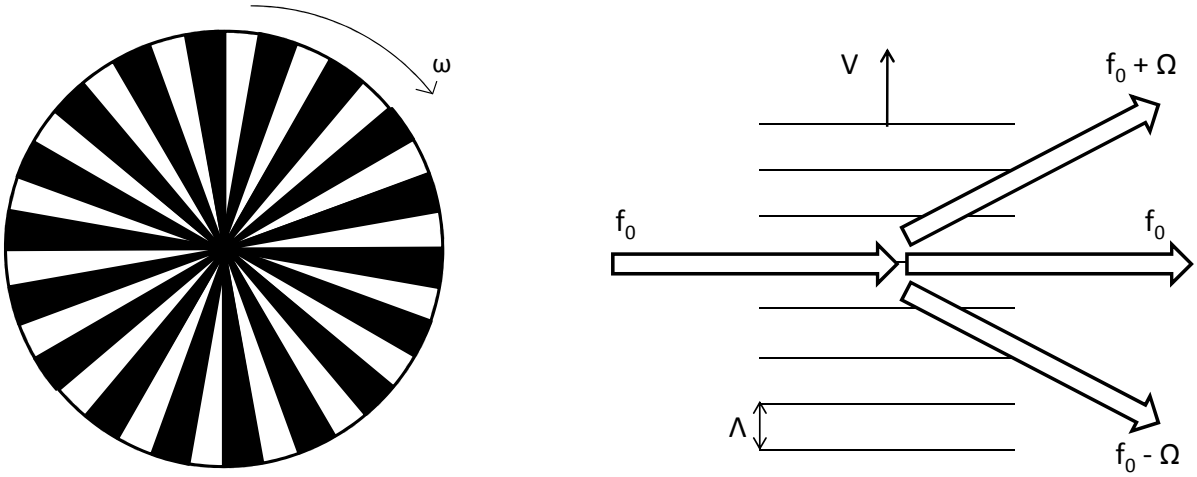

(a) ω = angular frequency

(b) f_0 = frequency of incoming light; Ω, Λ and V are the frequency, pitch and speed of the acoustic wave.

Figure 2.6: Diffraction based OFSs

to a fraction of the wavelength. The quadrature homodyne detection brings a solution to this problem, but still this configuration is working near DC and suffers from 1/f noise, limiting its performance.

One more component is needed for the heterodyne technique: an optical frequency shifter (OFS). The advantage of introducing this component is that the useful signal can be translated to a frequency band where less noise is present, which improves performance. Only one detector is needed.

2.3 Components of a heterodyne LDV

2.3.1 Optical frequency shifter

An optical frequency shifter (OFS) is needed for heterodyne detection. In this section we discuss how they look like. Generally, OFSs are based on diffraction upon moving gratings. The movement of the grating constitutes the frequency shift.

Rotating grating A rotating radial diffraction grating (Fig. 2.6(a)) produces an optical frequency shift. This OFS was first proposed in 1967 [13]. To understand the behaviour of a rotating grating, a linear grating moving perpendicular to the rulings and in the same plane as the grating will be first considered. Assume a cosine-like transparent grating with pitch a and moving with speed v. The transmission function is

$$T(x,t) = \frac{1 + \cos\left[\frac{2\pi}{a}(x - vt)\right]}{2}. \tag{2.23}$$

The place coordinate parallel to the velocity is denoted as x. Suppose the grating is illuminated with a collimated monochromatic wave, normally incident. The resulting field $\psi(f_x, t)$ in the Fraunhofer regime (far field) can then be found by taking the spatial Fourier transform of the transmission function wrt. x.

$$\psi(f_x,t) = \frac{\delta(f_x)}{2} + \frac{1}{4}e^{-j\frac{2\pi}{a}vt}\delta\left(f_x + \frac{2\pi}{a}\right) + \frac{1}{4}e^{j\frac{2\pi}{a}vt}\delta\left(f_x - \frac{2\pi}{a}\right), \tag{2.24}$$

f_x is the spatial frequency ($f_x = 2\pi x/\lambda z$, z is the distance perpendicular to the plane of the grating). The light in the zeroth order is not changed, while in the +1 and -1 order the frequency is respectively increased and decreased by v/a. When the grating is not a perfect cosine-like grating, other orders will also exist. The diffraction spots appear at

$$\sin(\theta) = \frac{x}{z} = m\frac{\lambda}{a} \ (m \in \mathbb{Z}), \tag{2.25}$$

where m stands for the different diffraction orders. For a radial grating the speed v and the pitch a are dependent on the radius r as $v = \omega r$ and $a = Kr$, with K a proportionality constant. The frequency shift is thus ω/K (for the first order) and this is independent of position.

Bragg cell The Bragg cell is based on the acousto-optic effect. A sound wave forms a diffraction grating by compressing the material in which the sound wave travels, inducing a refractive index variation. This idea was first proposed in 1963 [14]. As for the rotating grating, the frequency shift will be the speed of the acoustic wave V divided by its pitch Λ(Fig. 2.6(b)). Thus, the frequency shift is the same as the frequency Ω of the acoustic

wave. The diffraction spots will be at (see also Eq. (2.25))

$$\sin(\theta) = m\frac{\lambda}{\Lambda}. \tag{2.26}$$

Combining this equation together with $V = \Omega\Lambda$ gives

$$\Omega = \frac{V\sin(\theta)}{m\lambda} \tag{2.27}$$

Since $\sin(\theta)$ should be large enough to be able to separate the different orders and V is on the order of a few thousands m/s, Ω is in the order of tens of MHz for the Bragg cell.

2.3.2 Frequency demodulation

In a heterodyne system, the signal looks like a frequency modulated signal, with carrier frequency equal to the optical frequency shift f_{FS} and frequency deviation equal to the Doppler shift $f_D(t)$. To retrieve the Doppler shift, we should frequency demodulate the signal. This can be done digitally or analogously. We briefly introduce the most common analog methods and give a reference for the interested reader. However, digital modulation will be used in this work and will be explained in more detail.

The most common analog FM demodulating electronic circuits are:

- The *phase-locked loop*. This is a control system which tries to adjust its phase to the incoming signal. The error signal is used to find the original signal back [15].
- The *quadrature detector*. The incoming signal is mixed with a 90° phase shifted copy of the signal. A DC term with the original signal and a term at the double of the carrier frequency are produced. The original signal is filtered out [16].
- The *Foster-Seeley discriminator*. It consists of an electronic filter which changes the amplitude of the signal as a function of frequency [17].

Digital frequency demodulation can be divided into 3 steps: sampling, frequency down-shifting and low pass filtering, and finally recovering of the original signal. First, the analog FM signal

$$r(t) = \cos(2\pi f_{FS}t + \varphi(t)) \tag{2.28}$$

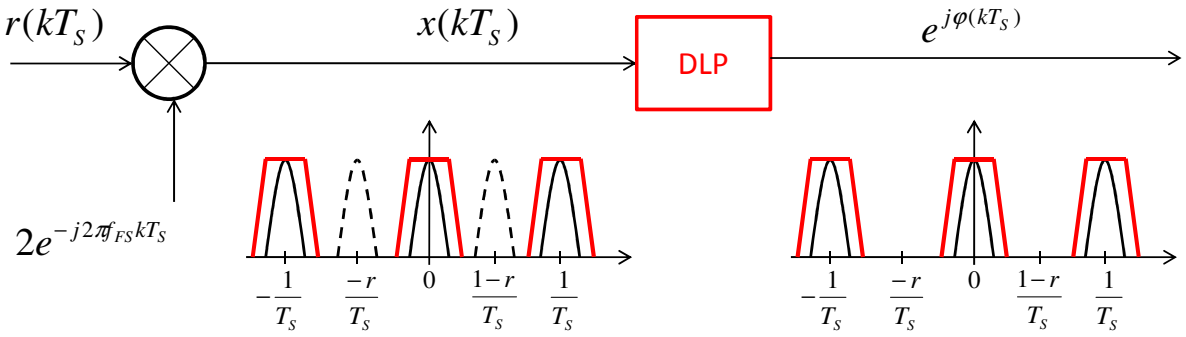

Figure 2.7: Overview of the first part of the demodulation.

is sampled. So t should be replaced by $0, T_S, 2T_S, \ldots$, where T_S is the sampling period. The sampled signal, written in complex format, is

$$r\left(kT_S\right) = \frac{1}{2}\left[e^{j\varphi(kT_S)}e^{j2\pi f_{FS}kT_S} + e^{-j\varphi(kT_S)}e^{-j2\pi f_{FS}kT_S}\right] \quad (k \in \mathbb{Z})\,. \tag{2.29}$$

The next part of the demodulation consists of bringing the useful signal to DC. This part is shown schematically in Fig. 2.7 and helps to understand the mathematical treatment below. The sampled signal is multiplied by $2e^{-j2\pi f_{FS}kT_S}$ to bring $e^{j\varphi(kT_S)}$ to DC. We get as new signal

$$x\left(kT_S\right) = e^{j\varphi(kT_S)} + e^{-j\varphi(kT_S)}e^{-j4\pi f_{FS}t}. \tag{2.30}$$

We separate $2f_{FS}T_S$ in its integer part $q \in \mathbb{Z}$ and fraction $r \in [0, 1[$. Then

$$x\left(kT_S\right) = e^{j\varphi(kT_S)} + e^{-j\varphi(kT_S)}e^{-j2\pi kr}. \tag{2.31}$$

The first term is centered at DC and aliases are found at multiples of the sampling frequency (solid lines in Fig. 2.7). The second term is centered at $-r/T_S$ and aliases are found at e.g. $(1-r)/T_S$ (dashed lines in Fig. 2.7). If we want both terms not to overlap in the frequency spectrum, r should be chosen around $1/2$. r close to 0 or 1 should be avoided, since then both terms will overlap. For $r = 1/2$, the sampling period should be

$$\frac{1}{T_S} = \frac{4f_{FS}}{2q+1}. \tag{2.32}$$

For $q = 0$, the sampling frequency should be 4 times the carrier frequency. The term $e^{j\varphi(t)}$ contains the information we are looking for. With a digital low pass filter we can delete

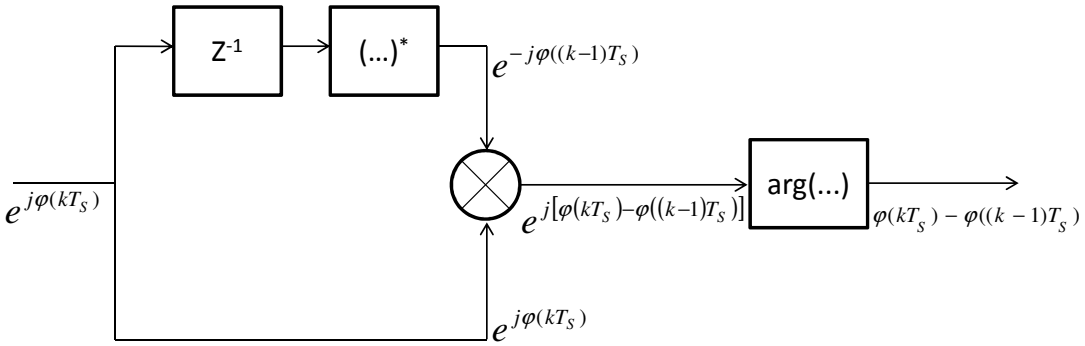

Figure 2.8: Overview of the second part of the demodulation.

the second term. The bandwidth of this filter should be smaller than $F_S/2$ to filter out the second term, but large enough in order not to filter out the signal. To eliminate noise as much as possible, the bandwidth of the filter should just accommodate the signal.

In the last part, the original frequency signal of $e^{j\varphi(t)}$ is obtained. The instantaneous frequency is related to $\varphi(t)$ as

$$f_D(t) = \frac{1}{2\pi}\frac{d\varphi(t)}{dt} \tag{2.33}$$

this translates into digital format as

$$f_D(kT_S) = \frac{\varphi(kT_S) - \varphi((k-1)T_S)}{2\pi T_S} \tag{2.34}$$

What follows to get $f_D(kT_S)$ is demonstrated in Fig. 2.8. The signal is multiplied with one that is delayed and complex conjugated. What drops out is $e^{j[\varphi(kT_S)-\varphi((k-1)T_S)]}$. By taking the argument of this and dividing through by $2\pi T_S$, we finally obtain the instantaneous frequency $f_D(kT_S)$.

A part of this frequency demodulating algorithm can also be used for homodyne quadrature detection. Recall that the output current of the 2 photodetectors are in quadrature for this detection method

$$I_x(t) \propto \cos(\varphi(t)) \tag{2.35}$$

$$I_y(t) \propto \sin(\varphi(t)). \tag{2.36}$$

With Euler's formula

$$e^{j\varphi(t)} = I_x(t) + jI_y(t). \tag{2.37}$$

This is exactly the same as what we get after the first part of the heterodyne demodulation. Hence, the second part of the heterodyne demodulation can be used to demodulate the homodyne quadrature signal.

2.4 Noise in LDVs

In this section we will give an overview of different noise sources in an LDV. Of all these noise sources, one is inevitably and leads to a fundamental limit of the smallest detectable vibration. This fundamental limit will be compared with the requirements for a middle ear microphone.

2.4.1 Laser linewidth

When the reference and measurement arm in an LDV have the same path length, the beams of both arms are perfectly coherent. The current at the detector oscillates then with frequency equal to the optical frequency shift f_{FS} (no vibration). If path length differs, the beams will become partially coherent. The instantaneous frequency in both arms can differ due to the linewidth of the laser. The photocurrent oscillates now with frequency $f_{FS} + \delta f\,(t)$, with $\delta f\,(t)$ caused by the path difference and the linewidth of the laser. This $\delta f\,(t)$ will be seen by the demodulator as a Doppler shift, disturbing our measurement.

We simulated the effect of the laser linewidth with *VPI*. *VPI* is simulation software for optical telecommunication systems. Nevertheless, it can also be used for our purpose since the software includes lasers, frequency modulators, detectors and signal processing. We built a model in *VPI* without any other noise sources and a perfect frequency shifter. The only non-ideal component is the laser, which has a non-zero linewidth and thus a finite coherence length L_c. Frequency demodulation of the photocurrent is done by the digital algorithm as explained in Section 2.3.2.

We swept the path difference in the LDV and recorded the output after demodulation, without any vibration applied. For equal arm lengths this output should be zero, while

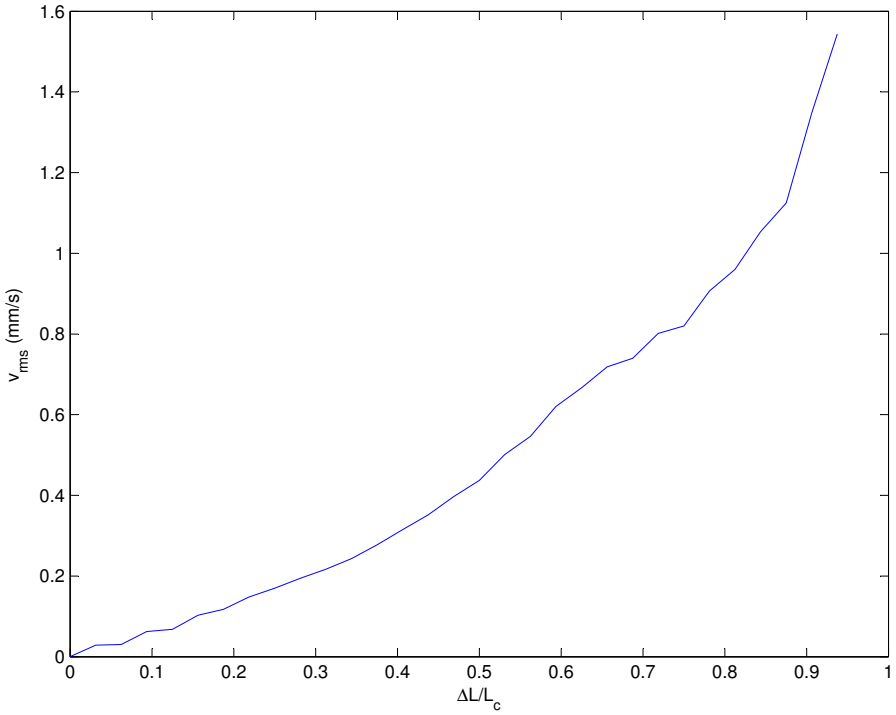

Figure 2.9: RMS value of the error speed as a function of the ratio between path length difference and coherence length

for different arm lengths this output becomes $\delta f\,(t)$. This corresponds to an error speed as $v\,(t) = \lambda \delta f\,(t)\,/2$. Results are given in Fig. 2.9. The root mean square of the error speed is given as a function of path length difference. For equal paths, the error is indeed zero, while for increasing path difference the error increases. For $\Delta L/L_c < 0.1$ the error speed is lower than 20 μm/s, for $\Delta L/L_c < 0.01$ the error speed is lower than 2 μm/s.

2.4.2 Other noise sources

RIN of the laser Relative intensity noise (RIN) describes the fluctuations in the output power of the laser. Even when a laser is provided with a constant current, the output power will fluctuate. The mechanism mainly responsible for this is spontaneous emission. A spontaneous emitted photon adds a small field component to the coherent field and perturbs both phase and amplitude randomly [2]. RIN is usually specified by the manufacturer of the laser as relative noise power in dB per Hz.

If the current is not stable, this will cause an extra noise factor, which can also be seen as a RIN.

Shot noise Shot noise is noise which is inevitably present at the conversion from an optical signal to an electrical signal. It is a quantum effect, which is related to the discrete nature of photons and electrons. The shot noise in the current for an optical signal with power P after falling on a detector with responsivity R is (RMS):

$$I_{sh} = \sqrt{2qRP_{DC}B} \tag{2.38}$$

with q the elementary charge, B the bandwidth in which is measured and $P_{DC} = P_m + P_r$ the constant part of the optical power.

Noise from the photodetector A photodetector produces noise because of the shot noise generated by its dark current (current generated without power falling on the detector) and by the thermal noise (see below) from its shunt resistance. The noise equivalent power adds up these noise sources and is defined as the power needed to generate a current equal to the noise current. Since it is dependent on bandwidth, it is usually expressed as a spectral density.

Thermal and amplifier noise The electronics following the photodetector will introduce noise. We discuss thermal and amplifier noise. Thermal noise results from thermal agitation of charge carriers in resistors. The noise voltage variance is

$$V^2_{thermal\ noise} = 4kTR\Delta f \tag{2.39}$$

or equivalent the current variance:

$$I^2_{thermal\ noise} = 4kT\Delta f/R \tag{2.40}$$

with kT the thermal energy, R the resistance and Δf the bandwidth in which the noise is measured.

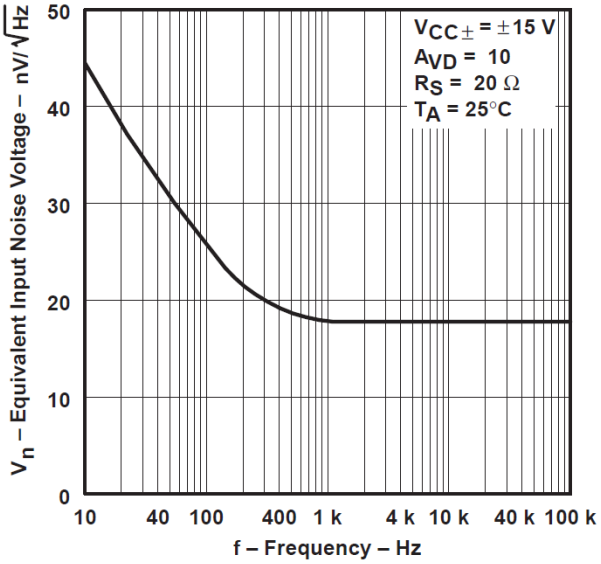

Figure 2.10: Noise characteristics of an amplifier (TL074)

For amplifiers, a noise voltage V_a is used, because it is dependent on bandwidth it is expressed as a noise spectral density, as in Fig. 2.10. It includes all different noises present in the amplifier. Note that for the amplifier in Fig. 2.10 1/f noise dominates at frequencies lower than 1kHz.

2.4.3 Shot noise limited operation

Eventually, we want to detect the minute vibrations in the middle ear. In this section we will try to deduce ourselves a minimum displacement we can measure with an LDV. We can then compare the smallest measurable displacement with the requirements of the ear microphone. This is a signal-to-noise-ration (SNR) problem: when noise becomes equal or larger than the signal, all information will be lost. A lot of noise sources are present in an LDV, but the only one we can not control by design is shot noise. With this fundamental noise, the smallest measurable displacement Δx_{min} can be retrieved. We will neglect all other noise sources, since they can be made smaller than shot noise by careful design.

The shot noise in the current is (RMS)

$$I_{sh} = \sqrt{2qR\left(P_m + P_r\right)B}. \tag{2.41}$$

From Eq. (2.6) and Eq. (2.20), one sees that the useful signal is contained in the oscillating part (RMS):

$$I_{signal} = \kappa R\sqrt{2}\sqrt{P_m P_r}, \tag{2.42}$$

where κ is the interference efficiency (related to the correct alignment of the polarization states of measurement and reference beam). So the SNR is

$$\text{SNR} = \frac{i_{signal}}{i_{sh}} = \sqrt{\frac{\kappa^2 R P_m P_r}{qB\left(P_m + P_r\right)}} \tag{2.43}$$

Looking back at Section 2.2.3, the spectrum of the signal consists of side peaks around the carrier frequency with separation equal to the vibration frequency (Eq. (3.6)). These side peaks actually contain the information about the vibration. When they are buried under noise, all information will be lost. Since for the detection limit $\Delta x_{min} << \lambda$ and

$$\beta = \frac{4\pi\Delta x_{min}}{\lambda} \tag{2.44}$$

β will be small. From Fig. 2.5 it can be seen that only the Bessel functions of zeroth and first order are important (Carson's rule confirms this: Eq. (2.22)). Following approximations for small β hold:

$$J_0\left(\beta\right) = 1$$

$$J_1\left(\beta\right) = \beta/2$$

Assuming equal magnitudes of noise and side peaks at $f_{FS} \pm f_{vib}$ for the detection limit Δx_{min}:

$$\frac{1}{2}\frac{4\pi\Delta x_{min}}{\lambda} = \frac{1}{\text{SNR}} \tag{2.45}$$

$$\Rightarrow \Delta x_{min} = \sqrt{\frac{qB\left(P_m + P_r\right)}{4\pi\kappa^2 R P_m P_r}}\lambda \tag{2.46}$$

We will now make a best case estimate for Δx_{min}. Since for vibrations in the middle ear the maximum displacement is smaller than the wavelength, the spectrum will only contain two side peaks. The minimal bandwidth needed around the carrier frequency is then twice the maximum vibration frequency, which is 6kHz (see Chapter 1). To minimize

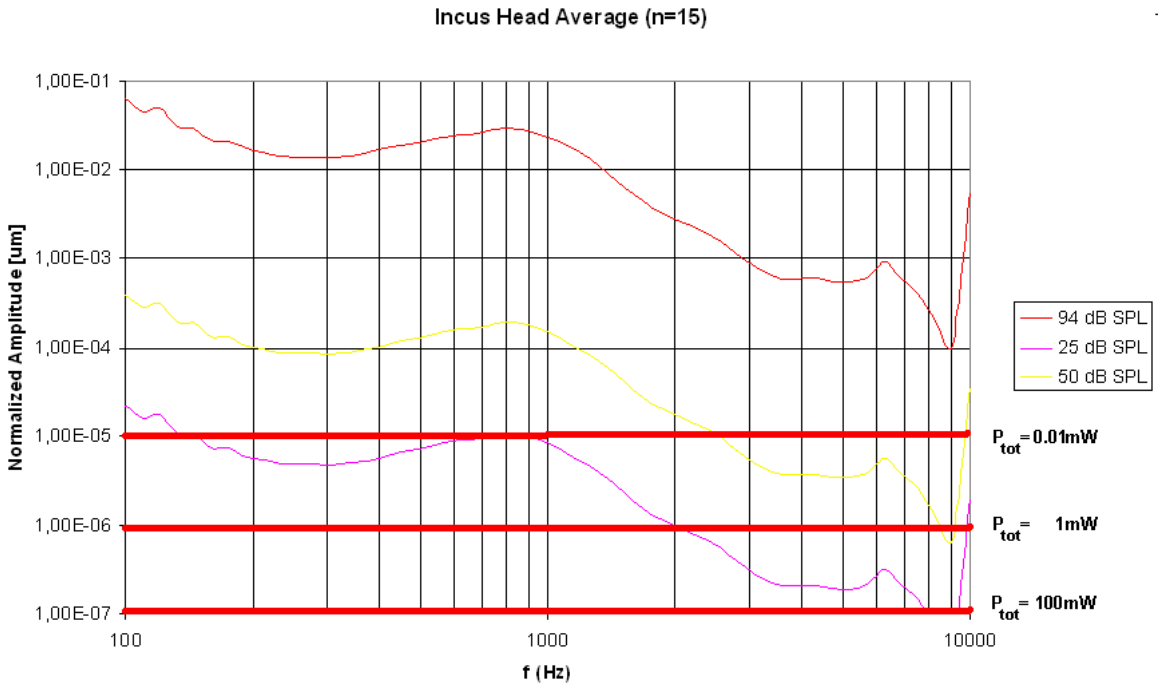

Figure 2.11: The detection limit for different values of the total power falling on the photodetector compared with displacement data for the incus head as a function of frequency of the sound. Data obtained from *Cochlear*.

the detection limit power should be equally divided between measurement and reference arm ($P_m = P_r = P_{total}/2$). For light with wavelength $\lambda = 1550$nm, R can be estimated as 1A/W and ideally κ is equal to 1. In this best case Eq. (2.46) is only dependent on the total power P_{total} falling on the detector,

$$\Delta x_{min} = \sqrt{\frac{qB}{\pi R P_{total}}}\lambda \tag{2.47}$$

The calculated detection limit is compared with displacement data for a bone in the inner ear for different total optical powers in Fig. 2.11. For a total power of 100μW, Δx_{min} is 10pm. With this minimal measurable displacement we can not measure the vibrations in the middle ear at 25dB SPL. Even at 50dB SPL, displacements with frequency higher than 3kHz can not be measured. Increasing the total power with a factor of 100 lowers Δx_{min} with a factor of 10. We can see on the graph that a total power of 1mW is still too low. Only for a power of 100mW the total targeted measurement range can be reached, which is much beyond the power budget.

2.5 Conclusion

We discussed homodyne and heterodyne detection to recover the Doppler shift. The homodyne technique needs a constant path difference control down to a fraction of the wavelength. An alternative, homodyne quadrature detection, circumvents this problem by using two photodetectors (instead of one) where signals are in quadrature. The heterodyne detection seems the best choice in terms of noise. The signal can be translated to a frequency band where less noise is present, whereas both homodyne techniques will suffer from 1/f noise. We considered possible noise sources and were able to derive a fundamental limit for LDVs based on shot noise. The fundamental limit showed that the weakest vibrations in the middle ear can only be measured for a power on the detector higher than 100mW, already 100 times larger than the targeted power budget. Admitting other noise sources as 1/f noise would only worsen this.

Chapter 3

Towards an integrated LDV on SOI

From previous chapter, we know that heterodyne detection suffers from noise the least. In this chapter, an integrated heterodyne LDV is proposed. The OFS is realized by serrodyne frequency shifting. Imperfections of this shifting technique are discussed, together with its influences on the performance of LDVs.

3.1 Silicon-on-insulator LDV

Recall from Chapter 1 that the ultimate goal is to develop a fully integrated LDV on silicon-on-insulator (SOI). In SOI technology, the light is guided in silicon. The Si guiding layer lies on SiO_2 and is surrounded by air at the top. The waveguide structure can have submicron dimensions. The refractive index of Si is much higher than air and SiO_2. This high index contrast allows sharp bends and hence small structures. Si is a relative cheap material and can benefit from the Si processing knowledge acquired in the electronics industry.

In previous chapter we derived that even in shot noise operation, the light power on the detector should be 100 times larger than the targeted power budget. To approach this fundamental limit as close as possible, other noise sources should be minimized. Homodyne detection is therefore not appropriate: it suffers from 1/f noise. Heterodyne detection, in contrast, offers the option to shift our signal to a frequency band where less

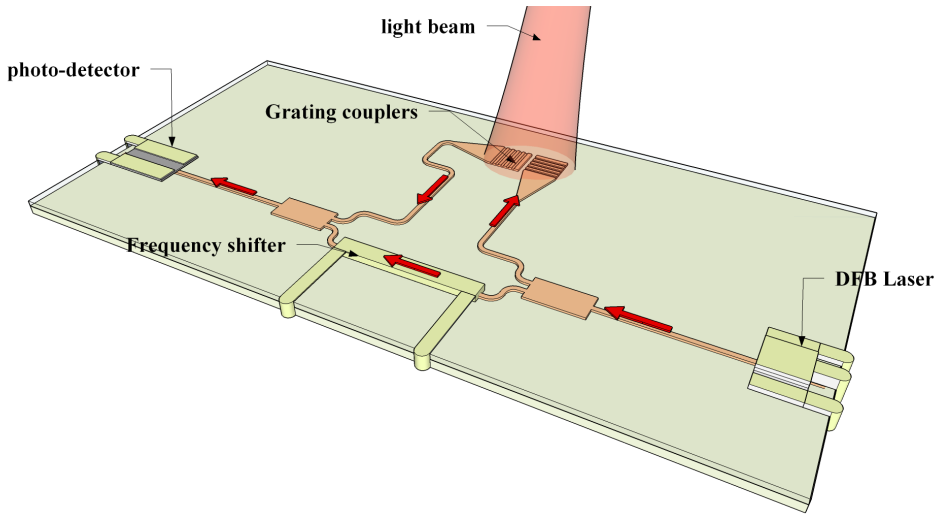

Figure 3.1: Outlook of an integrated LDV.

noise is present. A heterodyne LDV on SOI can then look like as in Fig. 3.1. Laser light is split into a frequency shifting arm and a measurement arm. Light from the measurement arm can leave the photonics chip through a grating coupler and is focused at the vibrating object. Another grating coupler can collect the reflected light back. Light from both arms is combined and falls on a photodetector.

Light sources and detectors in Si are not available with sufficient efficiency. However, hybrid integration of III-V semiconductors onto SOI brings a solution: lasers and detectors made of III-V compounds are bond to the SOI [1]. The last part needed is an OFS. Diffraction based OFSs, as discussed in 2.3.1, are too bulky to be integrated. A surface acoustic wave (SAW) OFS is based on the same principle as a Bragg cell: a moving sound wave diffracts the light to another frequency. The sound wave is situated at the surface of the chip [18]. However, this technique is not mature enough yet, since the conversion efficiency is still low.

3.2 OFS on SOI using serrodyne frequency shifting

Another option to realize the OFS is serrodyne modulation. Serrodyne frequency shifting (SFS) is accomplished by applying a sawtooth phase modulation to the optical signal.

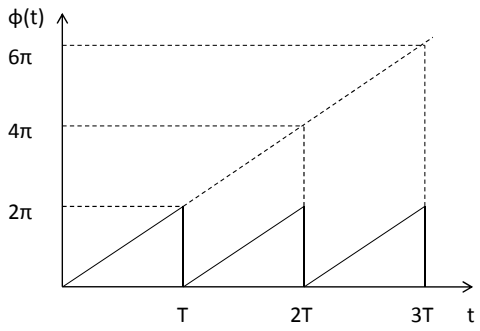

Figure 3.2: Ideal sawtooth for SFS.

Ideally, the sawtooth should change from 0 to 2π linearly and should have an infinitely short fall time (Fig. 3.2). Because there is no difference between a phase of 0 and 2π, the phase φ seen by the modulated light can then be written as

$$\varphi(t) = 2\pi \frac{t}{T}. \tag{3.1}$$

The realized frequency shift will be

$$\begin{aligned} f_{FS} &= \frac{1}{2\pi} \frac{d\varphi(t)}{dt} \\ &= \frac{1}{T}. \end{aligned} \tag{3.2}$$

Different phase modulation techniques are at forehand on SOI, the most important are discussed below.

Thermo-optic effect A heater is placed in the proximity of a waveguide. The heater is made of a resistive material and heat can be produced by the Joule effect. When a voltage is applied to the heater, the resulting change in temperature effectuates a change of effective index of the light in the waveguide. So by altering the voltage the phase can be changed. Thermal effects are rather slow and the bandwidth for this kind of phase modulation is limited to the MHz range. In addition, the power consumption is relatively high. However, this effect has been used to generate an optical frequency shift of 1kHz [19].

Electro-optic effect The application of an electric field to a material can result in a refractive index change. The Pockels effect, also known as the linear electro-optic effect,

causes a change in the real part of the refractive index Δn_i proportional to the applied field. This change can be described by the coefficients p_{ij}, which are dependent on the direction of the applied field compared to the crystal axes x, y and z:

$$\Delta n_i = \sum_{j=x,y,z} p_{ij} E_j \ \ (i = x, y, z)\,. \tag{3.3}$$

However, the centro-symmetric crystal structure of Si dictates that this effect disappears for (unstrained) Si.

The Kerr effect is the second order electro-optic effect. The change in real refractive index is proportional to second order terms of the electric field and described by the coefficients r_{ijk} as

$$\Delta n_i = \sum_{j,k=x,y,z} r_{ijk} E_j E_k \ \ (i = x, y, z)\,, \tag{3.4}$$

which is also dependent on the direction of the field. This effect is present in Si, although it is very weak.

Carrier injection/depletion Free carriers can absorb photons in Si. They absorb the energy of a photon and are then excited in their band. Kramers-Kronig's relation says that absorption and refractive index of a material are related with each other. So, by changing the concentration of free carriers, the absorption in the material is changed and eventually the refractive index.

Carrier injection/depletion phase modulation is based on this principle. Modulation bandwidths as high as 10GHz with low power consumption are reported [20].

3.3 Non-ideal serrodyne frequency shifting

Different deviations can occur from the ideal sawtooth in Fig. 3.2:

- fall time is not 0,
- phase changes from 0 to $2\pi(1 \pm \epsilon)$,
- nonlinearity in the ramp of the sawtooth.

Due to the periodic nature of the sawtooth phase modulation, any of these deviations will cause a conversion of the optical signal into spurious sidebands at multiples of f_{FS}.

3.3.1 Non-idealities in SFS

We will now examine the different periodic non-idealities of SFS, or in other words the implications of deviations from the ideal sawtooth. We can take advantage of the periodicity of the sawtooth to model the non-idealities as suggested in [21]. If the incoming light can be represented as $E_0 e^{j2\pi f_0 t}$ the phase modulated signal can be written as

$$E_0 e^{j[2\pi t f_0 t + \varphi(t)]} = E_0 e^{j2\pi f_0 t} \cdot \sum_{n=-\infty}^{+\infty} a_n e^{j\frac{2\pi n t}{T}}. \tag{3.5}$$

The sum in this equation denotes the Fourier series of $e^{j\varphi(t)}$. If the sawtooth is perfect ($\varphi(t) = 2\pi t/T$), only a_1 will be different from zero and be equal to 1. This corresponds with a perfect frequency shift. When the sawtooth differs from this situation we can still calculate this Fourier series, as long as the signal stays periodic. In this situation, other harmonics will emerge. The Fourier coefficients a_n can be calculated by:

$$a_n = \frac{1}{T} \int_0^T \exp\left(j \left[\varphi(t) - \frac{2\pi n}{T} t \right] \right) dt. \tag{3.6}$$

From these coefficients we can know how much optical power is translated to spurious sidebands. For example $|a_2|^2$ shows how much power is present in the sideband at twice the desired frequency shift.

Finite fall time The finite fall time non-ideality can be modeled as a piecewise linear function. The instantaneous fly back is replaced by a linear decrease which takes the fall time to get back to zero (Fig. 3.3(a)). The Fourier coefficients from Eq. (3.6) can then be calculated analytically. In Fig. 3.3(b) the sideband power, as $20\log\left(|a_n|^2\right)$, is plotted as a function of ratio between fall time and sawtooth period. As can be seen, the conversion efficiency reaches 100% when the fly back time goes to zero. The power in the nearest sidebands of the frequency shift is equally divided.

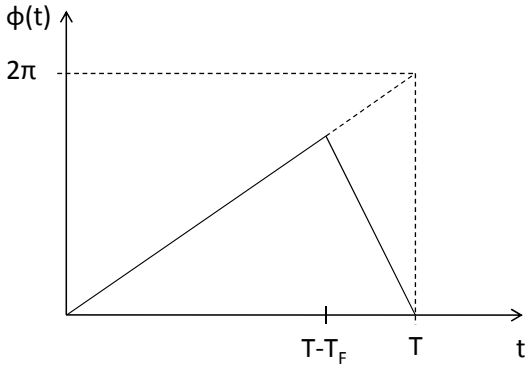

(a) Model for the fall time issue. T = period of sawtooth; T_F = fall time.

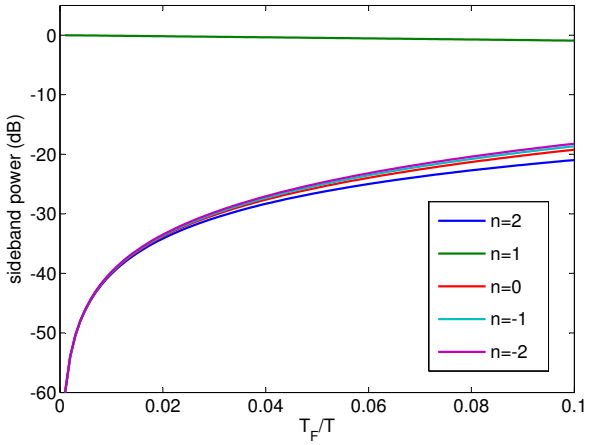

(b) Sideband power as a function of the ratio between fall time and sawtooth period. n=1 corresponds with the desired frequency shift.

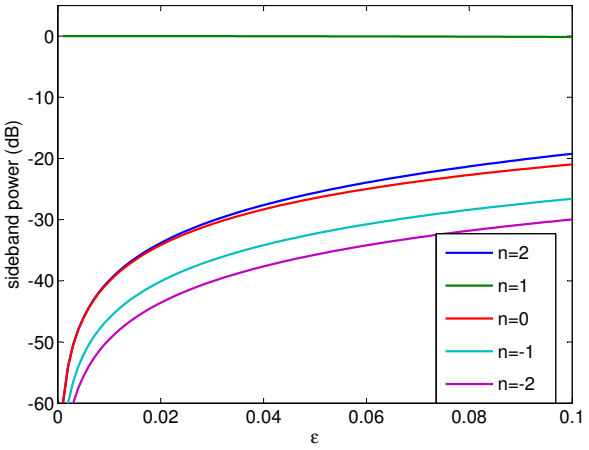

(c) Sideband power as a function of ϵ. n=1 corresponds with the desired frequency shift

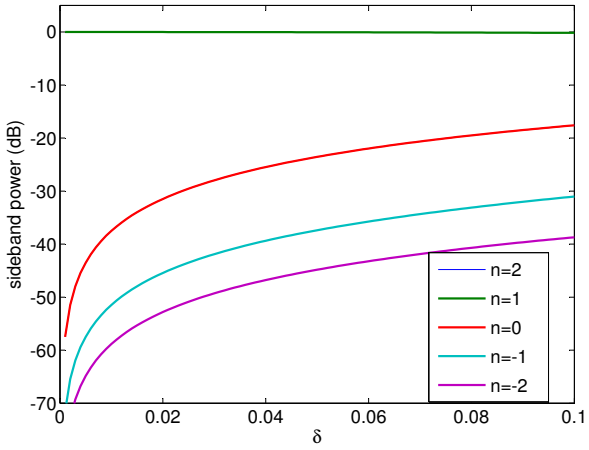

(d) Sideband power as a function of δ. n=1 corresponds with the desired frequency shift, n=2 and n=0 fall together.

Figure 3.3: Non-idealities of SFS.

2π deviation For this non-ideality, the non-ideal phase change can be written as:

$$\varphi(t) = \frac{2\pi(1+\epsilon)}{T}t. \tag{3.7}$$

At the end of the sawtooth period, the phase is a fraction ϵ higher than 2π. The Fourier coefficients can be calculated analytically again. In Fig. 3.3(c) the sideband power is graphed as a function of ϵ. The other case with $-\epsilon$ instead of $+\epsilon$ has similar results. The power in the sidebands is mainly concentrated in the nearest sidebands ($f = 0, 2f_{FS}$).

Nonlinearity in the ramp The phase change can now be modeled for example by

$$\varphi(t) = 2\pi\left[\frac{t}{T} + \delta\left|\sin\left(\frac{\pi t}{T}\right)\right|\right]. \tag{3.8}$$

This is a superposition of a perfect sawtooth and the absolute value of a sinusoid, which represents the non-linearity in the ramp. The modeled non-linearity will be largest in the middle of the period: the phase there is now $2\pi(1/2+\delta)$ instead of π. At the edges of the period the non-linearity is zero. Thus δ is a measure for the nonlinearity. The Fourier coefficients are now calculated numerically. The sideband power for varying δ is given in Fig. 3.3(d). Also here the power in the sidebands is mainly concentrated in the nearest sidebands ($f = 0, 2f_{FS}$).

3.3.2 Influence of non-ideal SFS on a LDV

In Section 3.3.1 different non-idealities of the SFS were examined. Different deviations from the ideal sawtooth resulted in spurious sidebands at multiples of the desired frequency shift. The question which arises is how this affects the performance of our complete system. We first describe what happens mathematically and compare these considerations with simulation.

Mathematical treatment of non-ideal SFS in an LDV

After non-ideal SFS, the frequency of the light f_0 is shifted to frequencies $f_0 \pm mf_{FS}$,

with magnitudes dependent on the degree of non-ideality. The electric field there is

$$E_r(t) = \sum_{n=-\infty}^{\infty} E_n \cos\left(2\pi\left(f_0 + nf_{FS}\right)t + \theta_n\right). \tag{3.9}$$

The electric field in the measurement arm is

$$E_m(t) = E_m \cos\left(2\pi f_0 t + \varphi(t)\right), \tag{3.10}$$

with $\varphi(t)$ the time varying phase due to the vibration of the object under interest. Combination of the light from both arms results in detected frequencies at the photodetector centered around $\ldots, -2f_{FS}, -f_{FS}, 0, f_{FS}, 2f_{FS}, \ldots$ In the ideal case only a frequency band around f_{FS} is present and a filter in the frequency demodulator filters out this band. Assume that this filter's passband is small enough to delete other frequency bands like e.g. around $2f_{FS}$. This requirement is in general fulfilled, since the DC component should be filtered out and the bandwidth of the filter should therefore be smaller than f_{FS}. Then, only two frequency bands will remain: one at f_{FS} and another, undesired one at $-f_{FS}$. We will only consider the electric fields which contribute to these frequencies, we assume the others are filtered out completely. The current at the photodetector is proportional to the square of the electric field

$$\begin{aligned} i(t) = [&E_m \cos\left(2\pi f_0 t + \varphi(t)\right) \\ &+ E_1 \cos\left(2\pi\left(f_0 + f_{FS}\right)t + \theta_1\right) + E_{-1}\cos\left(2\pi\left(f_0 - f_{FS}\right)t + \theta_{-1}\right)]^2. \end{aligned} \tag{3.11}$$

Only retaining frequencies which fall in the passband of the frequency demodulator gives

$$i(t) = E_m E_1 \cos\left(2\pi f_{FS} t + \varphi(t) + \theta_1\right) + E_m E_{-1}\cos\left(2\pi f_{FS} t - \varphi(t) - \theta_2\right). \tag{3.12}$$

We see that that both terms are centered at f_{FS}, but they are modulated with different sign! This will eventually lead to an error in the measurement. To see how the modulation is changed, we can use following trigonometric identity:

$$\begin{aligned} a\cos(x) + b\cos(x+\alpha) &= c\cos(x+\beta), \\ \text{with } c &= \sqrt{a^2 + b^2 + 2ab\cos(\alpha)} \\ \text{and } \beta &= \arctan\frac{b\sin(\alpha)}{a + b\cos(\alpha)}. \end{aligned} \tag{3.13}$$

With this, the photocurrent can be written as:

$$\begin{aligned} i(t) &= i\cos\left(2\pi f_{FS}t + \psi(t)\right), \\ &\text{with } i = E_m\sqrt{\left(E_1 - E_{-1}\right)^2 + 4E_1E_{-1}\cos^2\varphi(t)} \\ &\text{and } \psi(t) = \arctan\left[\frac{E_1 - E_{-1}}{E_1 + E_{-1}}\tan\varphi(t)\right]. \end{aligned} \tag{3.14}$$

For small E_{-1}/E_1, the modulation can be approximated to

$$\psi(t) \approx \left(1 - 2\frac{E_{-1}}{E_1}\right)\varphi(t) \tag{3.15}$$

From this equation we can conclude that for non-zero E_{-1}, the modulation will be smaller than it actually should be. So the spurious sideband at f_{FS} will lower the modulation and result in a lower measured Doppler shift. Notice that the factor is determined by the ratio the amplitude of the electric fields with frequency $-f_{FS}$ and f_{FS} and not the power ratio.

Simulation of non-ideal SFS in an LDV

The mathematical treatment will now be evaluated by simulation. *VPI*, the same software as used to study the influence of the laser linewidth (Section 2.4.1) will be used to simulate the non-ideal SFS. The serrodyne modulation is modeled by a general phase modulator driven with a non-ideal sawtooth. The vibrating surface is simulated by a frequency modulator which modulates with a frequency equal to the Doppler shift. We apply a single frequency vibration signal. This is measured by the LDV model with non-ideal SFS. The applied and measured signal are then compared by a root mean square error (RMSE) operation,

$$\text{RMSE} = \sqrt{\left\langle \left(\varphi_{\text{applied}}(t) - \varphi_{\text{measured}}(t)\right)^2 \right\rangle}. \tag{3.16}$$

To eliminate the influence of the magnitude of the vibration, this RMSE is divided by the root mean square (RMS) of the applied signal. Finally, the figure of resemblance (FOR)

$$\text{FOR} = 1 - \frac{\sqrt{\left\langle \left(\varphi_{\text{applied}}(t) - \varphi_{\text{measured}}(t)\right)^2 \right\rangle}}{\sqrt{\left\langle \varphi_{\text{applied}}(t)^2 \right\rangle}} \tag{3.17}$$

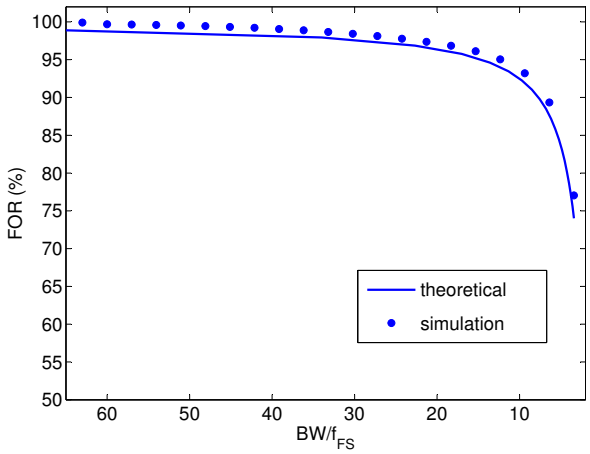

(a) Fall time

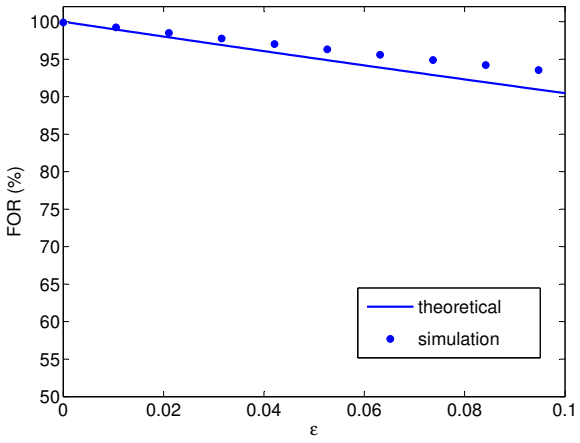

(b) Deviation on 2π

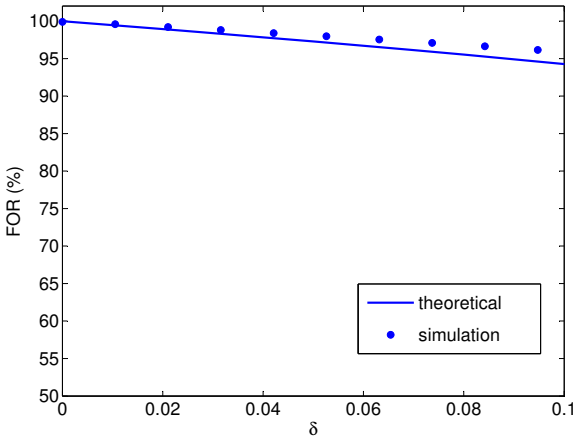

(c) Non-linearity in ramp

Figure 3.4: Influence of non-idealities in SFS on the FOR, calculated theoretically and by simulation.

is used to describe the similarity between applied and measured signal. Following Eq. (3.15) FOR should be 1-$2E_{-1}/E_1$, which can be calculated from the results for the different non-idealities in Section 3.3.1. The theoretical and simulated FOR for the different non-idealities are compared in Fig. 3.4.

In Fig. 3.4(a), the influence of the finite fall time of the serrodyne sawtooth is examined. In *VPI* this is simulated by passing the sawtooth through a low pass filter, which simulates the bandwidth of the phase modulator. This low passed sawtooth is then applied to an ideal phase modulator. The theoretical calculation follows the shape of the simulation well, the difference is less than 5%. The bandwidth requirement is stringent: if we want that

the measured vibration resembles the real vibration by more than 95%, the bandwidth of the phase modulator should be at least 20 times the frequency shift f_{FS}.

In Fig. 3.4(b) and 3.4(c) the 2π deviation (Eq. (3.7)) and the nonlinearity of the sawtooth (Eq. (3.8)) are studied. Again, the mathematical model and simulation are in good agreement. To have a FOR higher than 95%, the phase at the end of the ramp of the sawtooth should be contained in $[1.9\pi, 2.1\pi]$. The nonlinearity of the ramp should be limited to $\pm 0.2\pi$.

We can conclude that the theoretical calculation of the sidebands (Section 3.3.1) for these non-idealities and the corresponding measurement error (Eq. (3.15)) match well that from simulations, especially for small deviations from the ideal case.

3.4 Conclusion

In this chapter, we searched for a possible outlook of an integrated heterodyne LDV. Laser and detector can be integrated by bonding technologies [1]. However, an OFS is not readily available. As an alternative we proposed serrodyne frequency shifting. This technique needs a phase modulator driven by a sawtooth to realize the frequency shift. The imperfections of the serrodyne modulation creates spurious sidebands of which the sideband at $f_0 - f_{FS}$ deteriorates the signal. With the developed theoretical framework we can get an idea of how this influences the measured signal by the LDV.

Chapter 4

Realization of fiber based serrodyne LDV

In this chapter a macroscopic version of the proposed integrated LDV from previous chapter is built in fiber. We first evaluate the SFS and then conduct vibration measurements. These measurements will be compared with those obtained from a commercial LDV.

4.1 Experimental set-up

The experimental LDV set-up is shown in Fig. 4.1. It starts with a telecommunications distributed feedback laser. The laser is a DFB laser with 3dB linewidth of 2MHz, which corresponds with a coherence length of 150m. Light from this laser is split in a measurement and reference arm by a splitter. The serrodyne OFS is situated in the reference arm. Since this device is polarization sensitive, a polarization controller (PC) is inserted before it. In the measurement arm, light goes to the vibrating object trough an optical system which is discussed in more detail later. A coupler combines the light again. To maximize interference, a PC is placed in the measurement arm. The combined light falls on a telecom InGaAs photodiode. The photocurrent coming out of this photodiode is converted to a voltage by a transimpedance amplifier (TIA). Finally an analog-to-digital converter (ADC) transmits the created voltage to a personal computer. The frequency de-

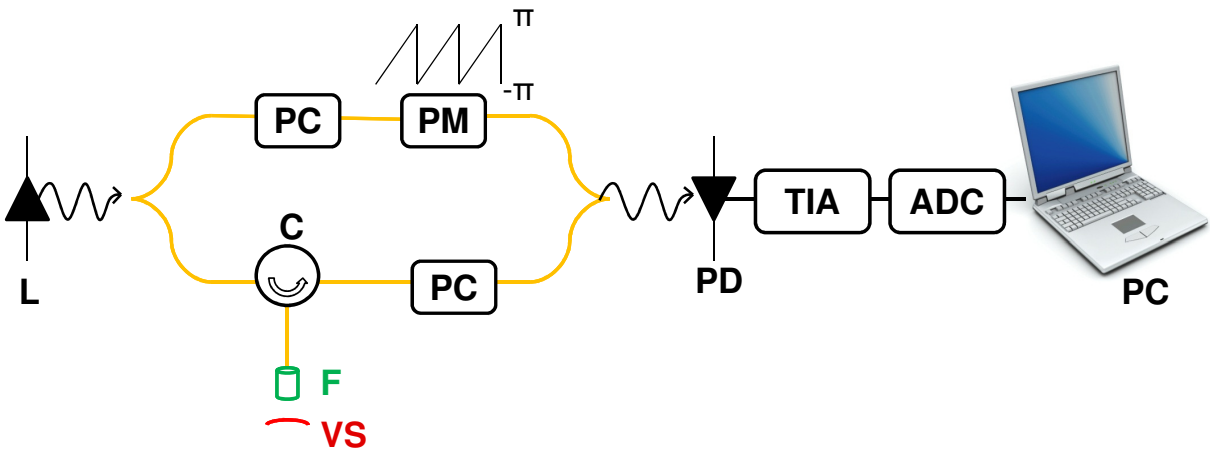

Figure 4.1: Overview of experimental LDV set-up. L = laser; PC = polarization controller; PM = phase modulator; C = circulator; F = focuser; VS = vibrating surface; PD = photodiode

modulation is done digitally. This gives more flexibility than an analog FM demodulator, because carrier frequency and bandwidth can be easily changed.

The own made design of the TIA can be found in Fig. 4.2. It mainly consists of three parts:

I reference voltage supply,

II the actual TIA and,

III a bandpass filter.

A universal adapter converts the AC of the electricity net to DC. The ground and 12V pin of the adapter feed the opamps in the rest of the design. Also a reference voltage is created by a voltage divider, which incorporates an RC low pass filter to filter out fluctuations in this reference voltage (0.4Hz cutoff frequency). A voltage follower is used as buffer.

In the second part we find the actual TIA. An incident power P_{in} will result in a photocurrent RP_{in}, with R the responsivity of the photodiode. The voltage after the TIA is related to P_{in} as,

$$V = R_F R P_{in}. \tag{4.1}$$

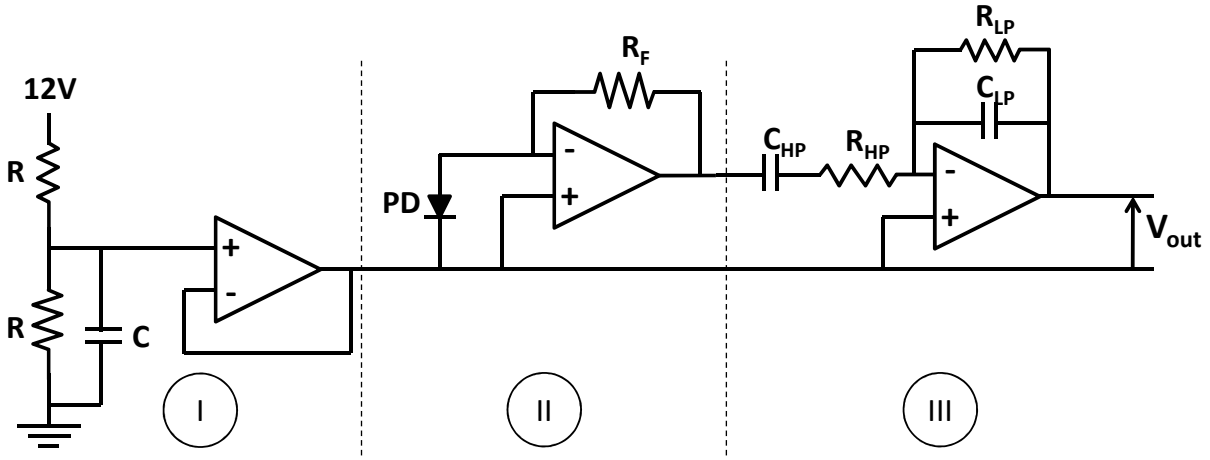

Figure 4.2: TIA circuit. I = reference voltage supply, II = actual TIA, III = bandpass filter, PD = photodiode, values of the components can be found in Tab. 4.1.

Part	Name of component	Value of component
I	R	10kΩ
	C	47μF
II	R_F	43kΩ
III	R_{HP}	39kΩ
	C_{HP}	100nF
	R_{LP}	51kΩ
	C_{LP}	33pF

Table 4.1: Values of components used in the TIA

We would like to digitize this voltage. Therefore, frequency components above half the sampling rate must be eliminated by a filter before sampling. Otherwise they will appear aliased in our sampled signal. The maximum sampling frequency of our computer is 192kHz and the cutoff frequency of the low pass filter is designed to be 95kHz. A high pass filter with cutoff frequency of 40Hz is placed to delete the DC component of the signal, which does not hold any useful information. When P_{in} falls in the passband of the filter, its corresponding voltage at the output will be

$$V_{out} = \frac{R_{LP}}{R_{HP}} R_F R P_{in}. \tag{4.2}$$

This corresponds with a conversion factor of 53mV/μW.

The TIA's output is connected to the microphone input of a computer. The soundcard serves as ADC and data can be captured and processed by the computer. The used soundcard works for frequencies from 1Hz to 48kHz. So, frequency shifts up to 48kHz can be recorded. The digital FM demodulation algorithm requires that $f_S = 4f_{FS}$, which is indeed fulfilled.

The phase modulator is a z-cut lithium niobate ($LiNbO_3$) modulator used for telecommunication purposes based on the electro-optic effect. This crystal shows a large electro-optic effect and phase modulation can be achieved by only applying a few Volts to it. The commercial phase modulator is normally used for high speed modulation (>GHz). For such high speeds, transmission line effects become non-negligible. To reduce reflections, a 50Ω terminating resistor is present in the design. However, as the modulation frequency goes down to megahertz range, heating effects with a smaller cutoff frequency come into play. The phase modulation is then affected by the thermo-optic effect. In order to use the phase modulator at low frequency (<10MHz), the terminating resistor is taken out to minimize the current in the electrodes and to get rid of the heating effect.

Because of the crystal structure of the modulator, the TM and TE mode inside it see a different phase modulation for the same voltage. The electro-optic for the TM mode is 6 times stronger than for the TE mode [22]. As a result, simultaneous input excitation of TM and TE mode can limit sideband suppression ratio. We want the TM mode to be

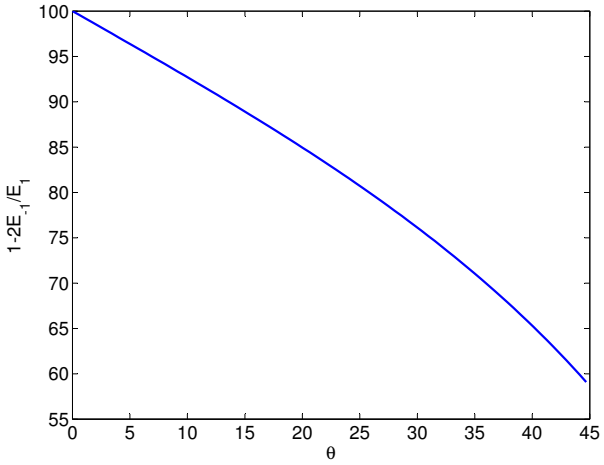

Figure 4.3: Modulation correctness for the polarization problem in the $LiNbO_3$ phase modulator as a function of θ.

excited, since this mode needs the least voltage to change the phase by π. The polarization of the input fiber should then coincide with the polarization of the TM mode. Spurious sidebands occur when polarization differs. As in previous chapter explained, we can calculate the power in the sidebands due to this polarization mismatch and the resulting error on the modulation by

$$\psi(t) \approx \left(1 - 2\frac{E_{-1}}{E_1}\right)\varphi(t)\,. \tag{4.3}$$

If we assume linear polarization in the fiber, this modulation error can be expressed as a function of the angle θ between TM mode and polarization of the fiber. In Fig. 4.3 this theoretical calculation is shown. The linear polarization of the fiber should make an angle smaller than 5° with the TM mode to have a resemblance in the modulation higher than 95%.

The procedure to select the correct polarization starts with disconnecting the measurement arm of the LDV. Only light in the reference arm is present. After the $LiNbO_3$ phase modulator, which is driven by a sawtooth to frequency shift the TM mode, we put a polarizer. When both TM and TE mode are excited, the polarizer will let both modes interfere since they received a different phase modulation. The polarization controller before the phase modulator is then adjusted until interference is gone. Only one mode

is excited in this case. By connecting the measurement arm again (no vibration) we can assess whether the TM mode (perfect sinusoid) or the TE mode (imperfect sinusoid) is selected.

4.2 Optical system at the object

Just pointing a fiber at the vibrating object will result in huge loss because of diffraction. A focuser can focus the light on the object and at the same time collect back reflected light. A circulator should then be inserted to separate the back reflected from the incoming light.

The larger the numerical aperture (NA), the more light can be collected. If the illuminated object is a Lambertian scatterer, the collected power by the focuser can be calculated. A Lambertian surface scatters the power following

$$P(\theta) = \frac{P_0}{\pi} \cos\theta, \tag{4.4}$$

with P_0 the total reflected power and θ the angle between the normal of the surface and direction of observation. The power collected by the focuser is

$$P_{foc} = \frac{P_0}{\pi} \int_{\Omega_{max}} \cos\theta d\Omega. \tag{4.5}$$

The maximum angle θ_{max} for which still power is collected is related to the NA as

$$\theta_{max} = \arcsin \mathrm{NA}. \tag{4.6}$$

Finally,

$$P_{foc} = \mathrm{NA}^2. \tag{4.7}$$

At first sight, we should maximize NA to get enough power back. However, oblique incident rays will experience another Doppler shift, because only the speed parallel to the direction of light contributes to the shift. If we again assume that the surface is a Lambertian scatterer, we can compare the Doppler shift for a certain NA with the real value of the shift when speed and light direction are parallel.

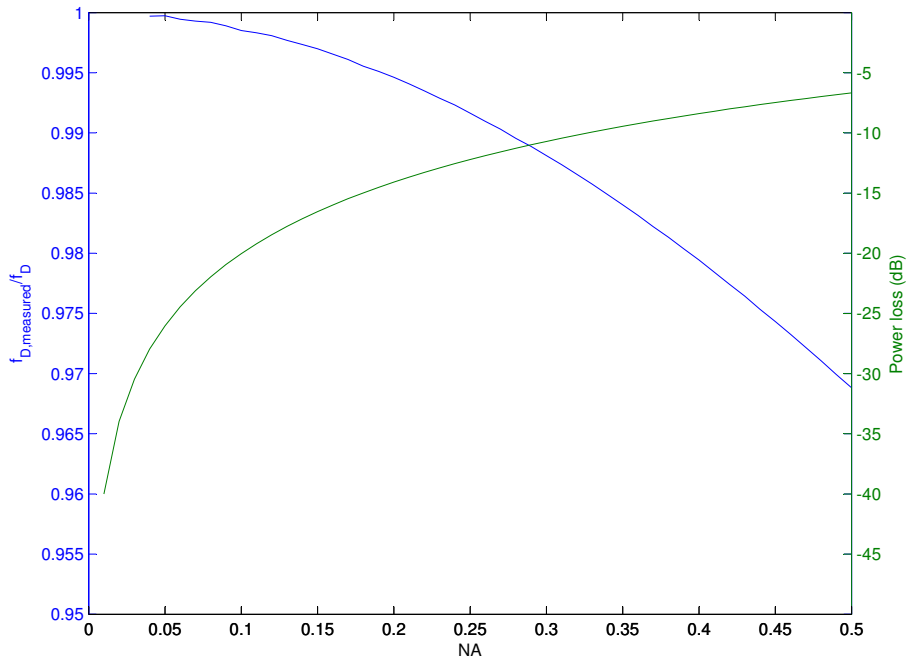

Figure 4.4: Blue: ratio between the measured Doppler shift with a focuser and real shift. Green: power loss of the focusing system for a perfect Lambertian scatterer. Both are plotted as a function of the NA.

All these calculations are summarized in Fig. 4.4. It is clear that there is a trade off for the value of the NA: a high NA gives lower losses, but also a higher deviation from the real Doppler shift.

Another problem faced when using a focuser is that due to the vibration of the surface, the surface becomes slightly out of focus. This will result in varying back reflected power. To see why this happens, look at Fig. 4.5(a). The beam diameter of the incident beam is a (equal to the beam diameter in the fiber) and focused to a spot with diameter Ma, where M is the magnification of the focuser. The magnification is the ratio of the distance from lens to image and the distance from the object to lens. For positions of the object slightly out of focus, the magnification will stay more or less the same. On the other hand, the spot size on the object will change to Ma'. This will result in a larger spot size a' in the object plane of which only the part falling in the diameter a is collected.

We can describe the spot size on the object as a function of the out of focus distance

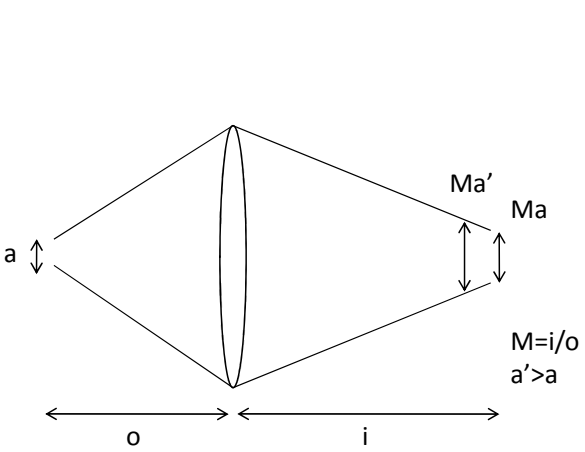

(a) Demonstrating the power loss when out of focus.

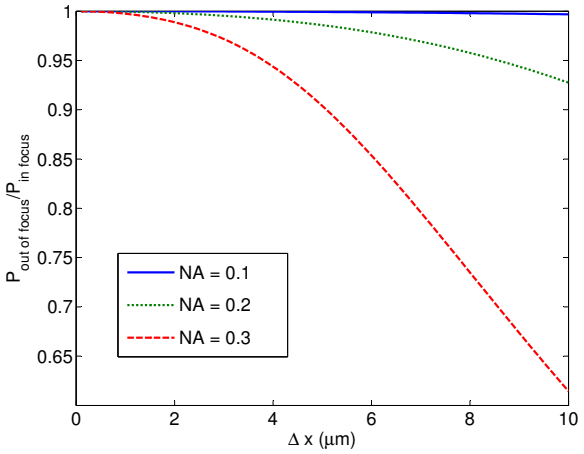

(b) The power loss when out of focus by an amount Δx.

Figure 4.5: Out of focus problem

Δx by using Gaussian optics

$$a'(\Delta x) = a\sqrt{1 + \left(\frac{\Delta x}{x_R}\right)^2}, \tag{4.8}$$

where $x_R = \lambda/\left(\pi \mathrm{NA}^2\right)$ is the Rayleigh range and related to the NA in the image plane.

The power loss when out of focus compared to when in focus as a function of out of focus distance Δx is given in Fig. 4.5(b). From this Figure we can deduce the power fluctuation for a certain vibration displacement and different NAs. For the same vibration displacement, a higher NA has higher losses since the Rayleigh range x_R is shorter. According to Eq. (4.8) the spot size on the object will become large, leading eventually to higher losses.

This implies that the power in the measurement arm is dependent on time. The photocurrent will change to

$$I(t) = \mathrm{DC} + 2\sqrt{I_r I_m(t)}\cos\left(2\pi f_{FS} t + \varphi(t)\right). \tag{4.9}$$

The carrier is now not only frequency but also amplitude modulated. However, this should not impose a problem as for frequency demodulation we are not interested in amplitude but frequency. With the frequency demodulation algorithm, the out of focus problem is

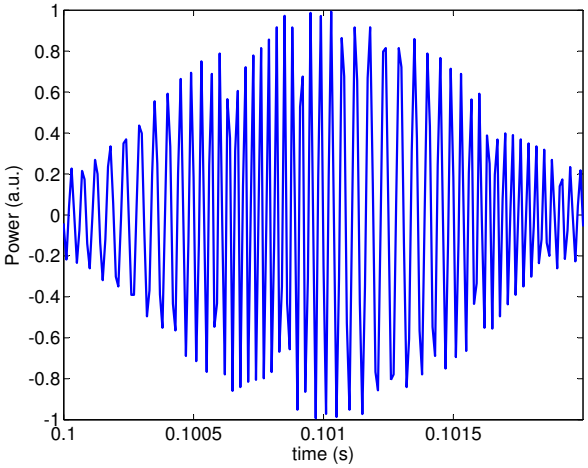

(a) Frequency modulated signal which is also amplitude modulated.

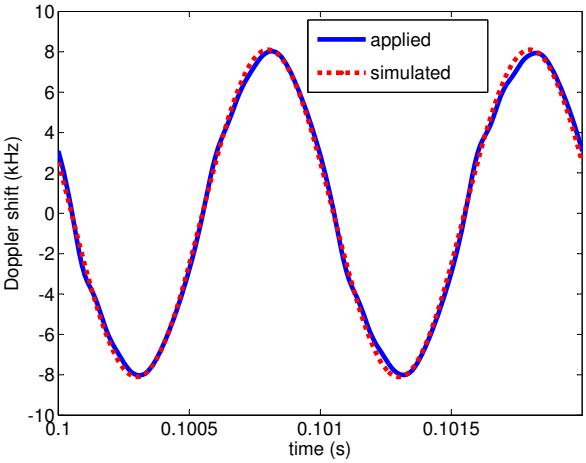

(b) The applied Doppler shift (dashed line) vs. the Doppler shift after demodulation (solid line).

Figure 4.6: Demonstration of insensitiveness of FM to AM

simulated. We apply a signal

$$I(t) = R(t)\cos(2\pi f_{FS}t + \varphi(t)), \tag{4.10}$$

with f_{FS}=25kHz, f_{vib}=1kHz and Δx=1μm. $R(t)$ denotes the power fluctuation caused by the focuser and we approximated it by

$$R(t) = 1 - \frac{R}{2}(1 + \cos(\pi f_{vib})), \tag{4.11}$$

R corresponds with the maximum loss caused by the focuser. Note that the loss oscillates with half the vibration frequency. In Fig. 4.6(a) the applied frequency modulated signal is plotted. We choose as an extreme case to put R equal to 0.95. The signal is amplitude modulated to less than one fifth of the full amplitude. In Fig. 4.6(b) the applied Doppler shift is compared with the Doppler shift obtained after demodulation. The demodulated version resembles the original. The frequency algorithm does not suffer from the amplitude modulation caused by the focuser, as long as there is a signal.

Besides these influences of the focuser's choice, there is also a practical side which should be taken into consideration: it should be not too difficult to focus the light on the object. The depth of focus (DOF) for a Gaussian beam is twice the Rayleigh range

$$\mathrm{DOF} = 2x_R = \frac{2\lambda}{\pi \mathrm{NA}^2}, \tag{4.12}$$

dependent on the NA of the focuser.

Taking everything from this section into account, we choose to work with a focuser with NA of 0.1. The DOF of this focuser is on the order of 100μm. The expected loss for a Lambertian surface is 20dB, while the deviation of measured Doppler shift and real shift is lower than 2%.

4.3 Serrodyne modulation results

4.3.1 Spurious sidebands of the SFS

Before starting vibration measurements, we will first look how good the SFS is. The different imperfections which can create spurious sidebands are:

- non-zero fall time,
- non-linearity in sawtooth ramp,
- deviation from 2π at end of sawtooth,
- different polarizations excited.

The signal generator which drives the phase modulator has a bandwidth of 1GHz, while the phase modulator has a bandwidth on the order of 10MHz. The limiting factor on the fall time is thus the phase modulator. For frequency shifts up to a few tens of kHz, the sideband suppression should be higher than 40dB.

The non-linearity issue can be studied by comparing the Pockels effect (first order electro-optic effect) with the Kerr effect (second order electro-optic effect). The Kerr effect is a second order effect and is a factor 1000 smaller than the Pockels effect. The non-linearity of the driving ramp is lower than 0.1%. Non-linearity effects will only cause sidebands more than 50dB lower than the desired frequency shift.

The voltage for a phase shift of π, V_π, is specified to be around 3.5V by the manufacturer of the phase modulator. To get a more accurate value for V_π we use our set-up as

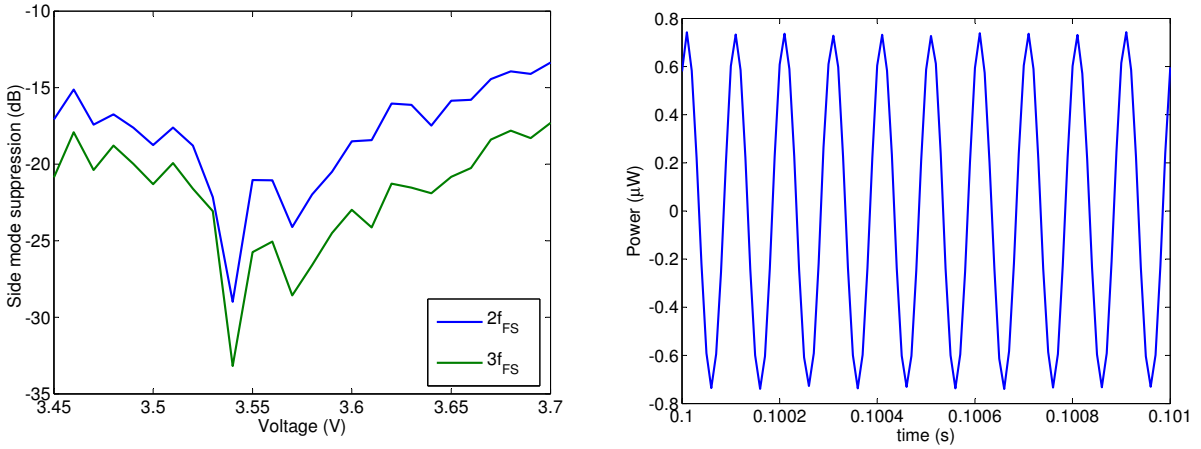

(a) Sideband suppression in dB ($=P_{nf_{FS}}/P_{f_{FS}}$) as a function of voltage V_π.

(b) Extract of interferometer output with V_π=3.54V. Sampling frequency is 100kHz.

Figure 4.7: In search for V_π

in Fig. 4.1 but with the optical system to the vibrating surface taken out and replaced by fiber. What we get is an interferometer with a SFS in one of the arms. We then change the voltage of our sawtooth modulation and take a look at the different spurious sidebands. Notice that we can not distinguish between positive ($f_{FS}, 2f_{FS}, \ldots$) and negative frequencies ($-f_{FS}, -2f_{FS}, \ldots$); the negative frequencies are folded over the positive frequencies. The side mode suppression, as the power at nf_{FS} divided through by the power at f_{FS}, as a function of voltage V_π is shown in Fig. 4.7(a). f_{FS} is 10kHz here, so that $2f_{FS}$ and $3f_{FS}$ fall in the bandwidth of the audio card. There is a minimum of the power in the side modes at V_π=3.54V. An extract of the waveform at the output of the interferometer is shown in Fig. 4.7(b). The side mode suppression is not monotonically decreasing towards the minimum at V_π=3.54V. The non-monotonicity indicates that this is due to small variations in polarization input to the phase modulator.

So we can not directly see the power at $-f_{FS}$, which tells us how modulation is affected. However, we can get an estimate by looking at $3f_{FS}$, since the side modes are rather symmetric around f_{FS} (see Fig. 3.3). Ignoring the fact that $-3f_{FS}$ is folded onto $3f_{FS}$, we estimate the power at $-f_{FS}$ to be -33dB the power at f_{FS}. With this corresponds a modulation error smaller than 95%.

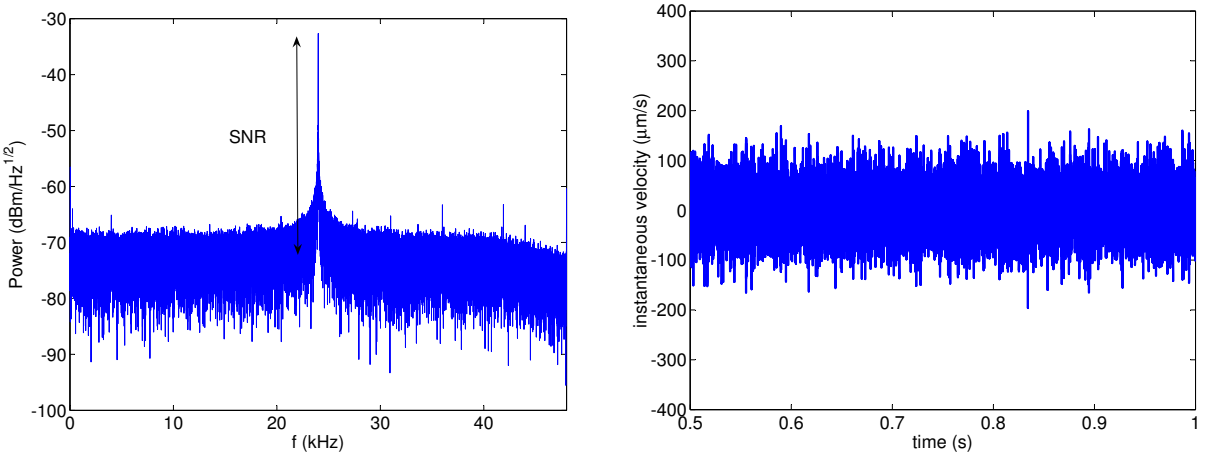

(a) Spectrum at output of interferometer, light power per Hz as a function of frequency. Interference efficiency κ=0.6.

(b) Extract of instantaneous speed after frequency demodulation.

Figure 4.8: Spectrum and noise equivalent instantaneous speed for a 24kHz shift.

4.3.2 SNR and noise equivalent speed

We will now work with f_{FS}=24kHz. This makes it easier to filter out the nearest sidebands. The spectrum of the interferometer is shown in Fig. 4.8(a). This is with a laser input of 7μW. The coupler splits this equally in upper and lower arm. The $LiNbO_3$ modulator induces a 3dB loss. At the detector 0.8μW from the arm with modulator is received, while 1.5μW in the arm without modulator (still without vibrating subject). The SNR for a spectral bandwidth of 1Hz is around 40dB. From now on, we will denote the SNR for a spectral bandwidth of 1Hz as SNR*. With this SNR* we can deduce the noise equivalent displacement as with Eq. (2.45),

$$\Delta x_{min} = \frac{\lambda}{2\pi}\frac{1}{\mathrm{SNR}}. \tag{4.13}$$

We have to take into account that the SNR in this formula is for the whole bandwidth in which we measure (12kHz), while the SNR* from the graph is for a spectral bandwidth of 1Hz. With the formula, we obtain a noise equivalent displacement of 3nm. A noise equivalent speed can be found by

$$\Delta v_{min} = 2\pi f_{max}\Delta x_{min}, \tag{4.14}$$

with f_{max} the maximum frequency which is not filtered out. In our case this is 6kHz and Δv_{min} becomes 100μm/s. The output after frequency demodulation is indeed in this range, see Fig. 4.8(b).

In shot noise limited operation the SNR* on the graph should be 90dB, however this is not the case. Where does the noise come from? We evaluate the different possible noise sources given in Section 2.4. We will convert the different noise sources to noise in optical domain, since the SNR* is also calculated in terms of light power.

Laser linewidth The linewidth of the laser is 2MHz, corresponding with a coherence length of 150m. The path difference between the arms of the LDV is made smaller than 1m, which corresponds with a noise equivalent speed lower than 2μm/s according to the simulations of Section 2.4.1. The laser linewidth can not be the reason of the limited SNR*.

Thermal noise The thermal noise due to the resistors in the TIA (converted to noise in light power) is

$$Noise(W) = \sqrt{4kT\left(\frac{1}{R_F} + \frac{R_{HP}}{R_F^2} + \frac{R_{HP}^2}{R_{LP}R_F^2}\right)}\frac{\Delta f^{1/2}}{R}. \tag{4.15}$$

This corresponds with a noise power of -90dBm/Hz.

Amplifier noise The amplifier noise voltage V_a is expressed as a noise spectral density for the opamps used in the design of the TIA. In the frequency region where we use the opamps V_a is equal to 18nV/$\sqrt{Hz}$. The amplifier current noise I_a is 0.01nA/$\sqrt{Hz}$. In terms of light power, the noise from the amplifiers in the TIA can be written as

$$Noise(W) = \frac{\Delta f^{1/2}}{K}[\frac{V_a^2}{R_F^2}\left(1 + \frac{R_{HP}^2}{R_{LP}^2}\right) + I_a^2\left(1 + \frac{R_{HP}^2}{R_F^2}\right). \tag{4.16}$$

This corresponds with a noise power of -93dBm/Hz.

ADC noise The noise from the soundcard, which serves as ADC, is recorded by short circuiting it. The noise power is measured to be around -85dBm/Hz.

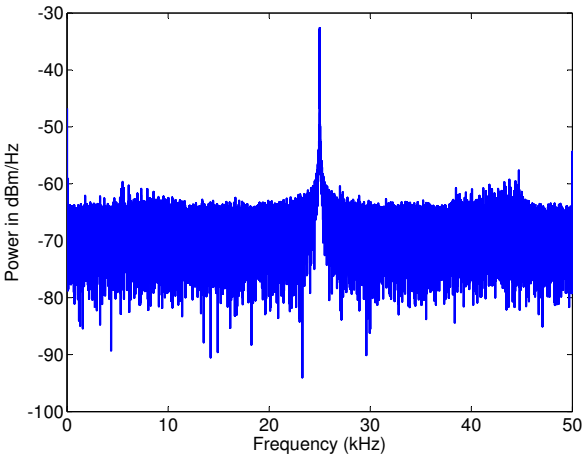

(a) Spectrum at output of interferometer, power at detector is 2μW.

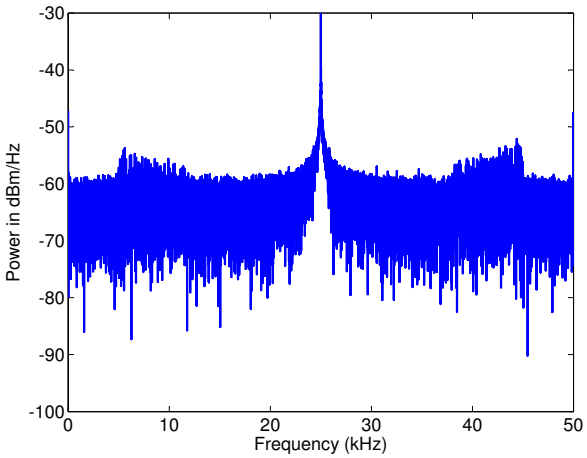

(b) Spectrum at output of interferometer, power at detector is 10μW.

Figure 4.9: Laser drive current noise.

Noise source	Noise in dBm/Hz for 2μW	Noise in dBm/Hz for 10μW
RIN	-148	-155
diode	-113	-113
shot noise	-91	-87
thermal noise	-90	-90
amplifier noise	-93	-93
ADC	-85	-85

Table 4.2: Different noise sources and their values for 2μW and 10μW on detector.

Laser current drive noise The noise in the current drive of the laser causes another relative intensity noise. In Fig. 4.9 the spectrum for different powers on the detector are plotted. The noise floor is for both of them higher than what we expect from previous noise considerations, see Table 4.2. We think the noise floor here is an effect of the noise in the current drive. This idea is proofed by using another current drive with higher current noise. The noise floor is then indeed raised. For the current drive used, the associated noise is $43\text{dB}/\sqrt{Hz}$ lower than the input power.

In conclusion, the noise floor observed is caused by noise from the current drive of the laser. Increasing the power on the detector will not increase SNR, since the associated

noise stays always 43dB/$\sqrt{Hz}$ lower than the input power. Of course the opposite is also true. We can lower the power without decreasing the actual SNR, until another noise source becomes significant. This will be the noise coming from the ADC.

A more stable current source should be used to get higher SNR. Another possible solution to delete the current noise problem is offered by balanced detection, which is used in coherent lightwave systems to reduce relative intensity noise from the laser[2]. A 3dB 2x2 coupler mixes the optical signal from both reference and measurement arm and splits the combined optical signal into two equal parts with a 90° relative phase shift of the electric field. At the end of each arm a photodetector captures the power, which is proportional to the square of the electric field. The photocurrents will be 180° out of phase:

$$I_+(t) = I_r + I_m + 2\sqrt{I_r I_m}\cos\left(2\pi f_{FS} t + \varphi(t) + \theta\right), \tag{4.17}$$

$$I_-(t) = I_r + I_m - 2\sqrt{I_r I_m}\cos\left(2\pi f_{FS} t + \varphi(t) + \theta\right). \tag{4.18}$$

The subtraction of I_+ and I_- provides the heterodyne signal. The DC term is eliminated completely during the subtraction process and its associated intensity noise vanishes.

4.4 Vibration measurements

4.4.1 Optimized SNR

The serrodyne modulation is good enough (an error smaller than 5% will be induced due to the non-idealities) to do real vibration measurements. However, the SNR* is limited to 40dB, which corresponds with a noise equivalent speed of 100μm/s. This limitation is caused by noise on the current drive of the laser, which can be treated as relative intensity noise. The SNR is then proportional to

$$\text{SNR} \propto \frac{\sqrt{P_m P_r}}{P_m + P_r}. \tag{4.19}$$

To obtain the highest possible SNR, power in measurement arm and reference arm should be equal. If the power is split equally in reference and measurement arm, the power in the

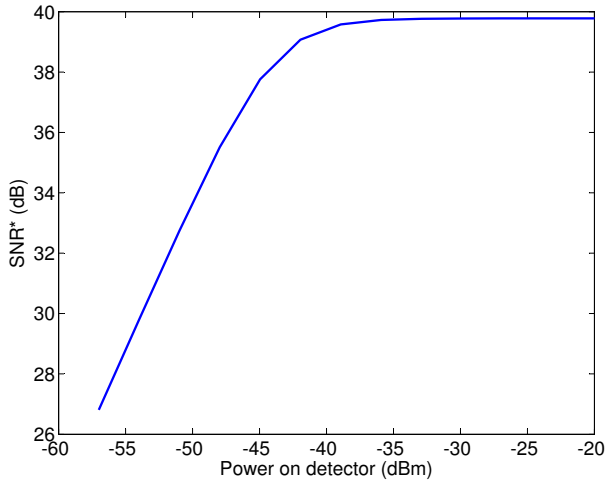

Figure 4.10: SNR* as a function of power on the detector.

measurement arm will be much lower than in the reference arm as a result of the losses at the focuser. Even with a retroreflective film on the vibrating surface, losses are around 20dB. Therefore, the 50:50 splitter after the laser is changed into a 99:1 splitter in order to have more equal power in both arms.

The SNR*, assuming equal power in both arms, is calculated in Fig. 4.10. For a total power falling on the detector higher than -40dBm (100nW) the SNR* is constant and determined by the current drive noise. For lower light powers, the noise from the ADC comes into play. This noise is constant and results in a decrease of the SNR* at a rate of 10dB/dBm.

4.4.2 Measurements of sound from loudspeaker

The vibration measurements will be executed on a loudspeaker. A retroreflective film is put on the membrane of the loudspeaker to get more light back. Still the power loss is around 20dB. We want to use as less power as possible, since the long term vision states that the LDV should have a low power consumption. From the SNR discussion in previous section, we know that the SNR* is limited to 40dB. For this, the power falling on the detector should be higher than 100nW. We will work with a total power of 200nW on the detector; 100nW comes from the measurement arm, another 100nW comes from the

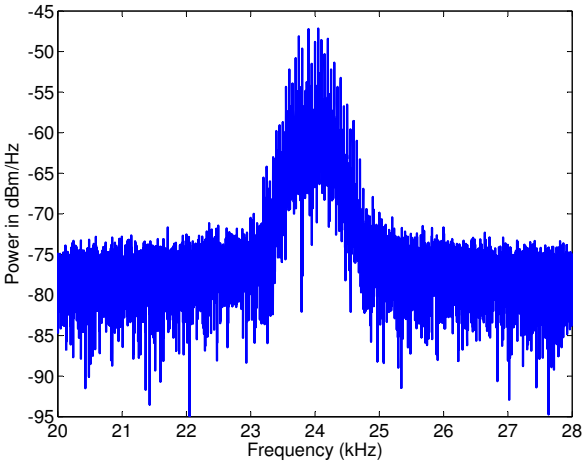

(a) Spectrum at output of interferometer, light power per Hz as a function of frequency, f_{FS}=24kHz.

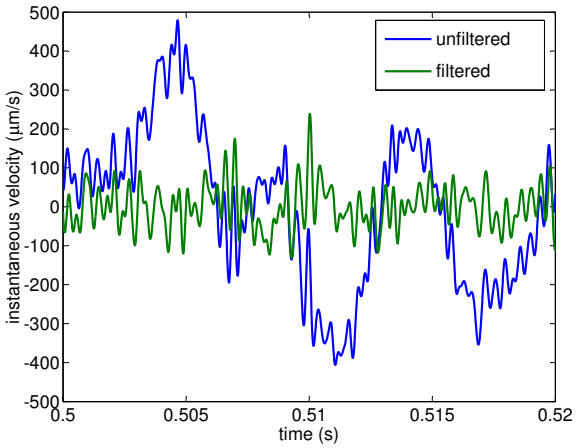

(b) Extract of instantaneous speed after frequency demodulation, with and without post filtering

Figure 4.11: Spectrum and noise equivalent instantaneous speed for a 24kHz shift.

reference arm. With these power levels in the arms the shot noise limited SNR* is 55dB, 15dB higher than our SNR* now. These power levels correspond with an input power of 50μW. However, for such low power level the light from the telecom laser is mainly due to spontaneous emission. Therefore, the output of the laser is adjusted to 5mW (well above threshold) and an attenuator (20dB) between the laser and input of the interferometer is inserted.

In Fig. 4.11(a) the spectrum at the output of the interferometer is depicted, the loudspeaker is muted. The noise floor (-80dBm/Hz) approaches the noise from the ADC (-85dBm/Hz), as expected. The peak at f_{FS} is broadened compared with the set-up from previous section, see Fig. 4.8(a). The large membrane from the loudspeaker picks up low frequency vibrations of the environment, resulting in side peaks in the spectrum. The 3dB width of the peak is on the order of 100Hz. The frequency range we are interested in is between 300Hz and 6kHz. We can separate these unwanted low frequency components from our frequency range by integrating a highpass filter after our demodulation algorithm with cutoff frequency equal to 300Hz. This is demonstrated in Fig. 4.11(b). The unfiltered demodulation output differs from the 100μm/s noise equivalent speed from

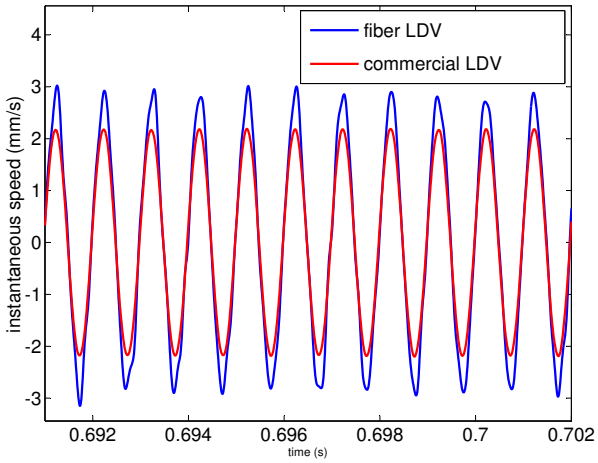

Figure 4.12: Fiber LDV and commercial LDV comparison.

previous section, it is corrupted with low frequency vibration. In contrast, the filtered output shows no low frequency vibrations and the noise equivalent speed equals 100μm/s again. The whole system will now only transmit frequencies between 300Hz (highpass filter) and 6kHz (filter in FM demodulation algorithm).

We will compare our fiber based LDV measurement of the vibrating loudspeaker with a commercially available LDV. This LDV from *Polytec* is free space based and employs heterodyne detection. The frequency shift is realized with a Bragg cell. The noise equivalent speed for this LDV is specified as 1μm/s for light falling on a surface with retroreflective film. This is lower than the noise equivalent speed of our set-up and hence we can use the commercial LDV as a reference. The size of the focuser (diameter=3cm) prohibits measuring simultaneously with fiber and commercial LDV. The monotone vibration of the speaker is measured separately with both devices.

First, we evaluate a vibration with speed larger than the noise equivalent speed of our set-up (100μm/s). Since we set the bandwidth around f_{FS} as 12kHz, we can not measure an infinitely large speed. From Carson's rule we know:

$$BW = 2\left(f_D + f_{vib}\right). \tag{4.20}$$

If we apply a sound with f_{vib}=3kHz, the speed should be lower than 4mm/s. In Fig. 4.12 a vibration with f_{vib}=3kHz and maximum speed of 2mm/s is measured. The periodic

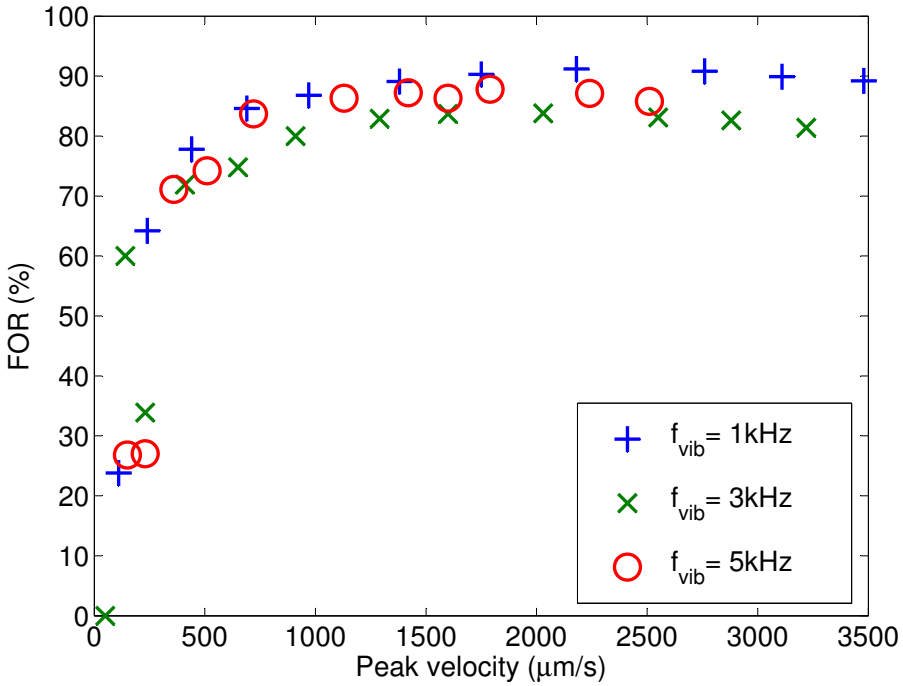

Figure 4.13: FOR for different vibrating frequencies and speeds, BW = 12kHz.

signals from both measurements are time shifted to let both signals fall together. Also, they are passed through the same filter to get rid of the low frequency components (as done in Fig. 4.11(b)). We see that both signals have the same periodicity, however the amplitude of the signal differs by a factor 0.76. A possible reason is that for the fiber LDV, the focuser is as close as 14mm, while the working distance for the *Polytec* LDV is 200mm. The close proximity of the fiber LDV's focuser may disturb the measurement.

Anyway, we can treat this error factor as a calibration factor and rescale our measurements with it. We define as figure of resemblance (FOR)

$$\mathrm{FOR} = 1 - \frac{\mathrm{RMS}\,(v_P - v_f)}{\mathrm{RMS}\,(v_P)}, \tag{4.21}$$

similar as the FOR defined in the computer aided design chapter. v_P and v_f are the vibration speed measured with Polytec's LDV and our fiber based LDV respectively. The calculated FOR for different vibration frequencies and speed are shown in Fig. 4.13. The trend for all vibration frequencies are the same. At speeds close to the noise equivalent speed the FOR is low. For a speed of 300μm/s the FOR is higher than 60%, and for speeds higher than 800μm/s the FOR transcends 80%. At even higher speeds the FOR

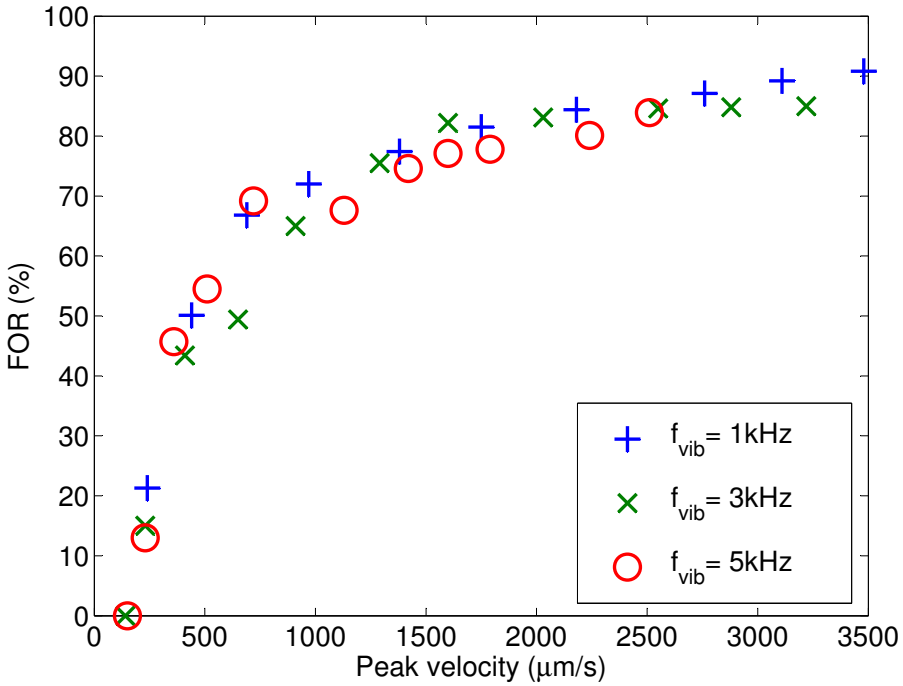

Figure 4.14: FOR for different vibrating frequencies and speeds, BW = 24kHz.

saturates and even drops slightly. This is because the bandwidth of our signal (Eq. (4.20)) becomes larger than the bandwidth (12kHz) around f_{FS}. Information will then be lost when filtering, resulting in distortions and lower measured speed.

We could change the BW to a higher value to solve this problem, but this will result in a higher noise equivalent speed. This is proofed by Fig. 4.14. The bandwidth is changed to 24kHz instead of 12kHz. The FOR is lower for low speed since the noise equivalent speed is higher. A FOR larger than 60% is obtained for 600μm/s and a FOR of 80% only for speeds higher than 2000μm/s. However, the drop for highest speeds in the measured range has now disappeared.

In a next experiment, we changed the retroreflective film on the loudspeaker to a piece of recycled paper. This recycled paper has lower reflection and can be thought of as an analogue to a bone in the middle ear. With this piece of paper we can thus study what happens when there are higher losses. For the retroreflective film the losses were around 20dB, for the paper losses are increased to 33dB, an extra of 13dB. If we still use an

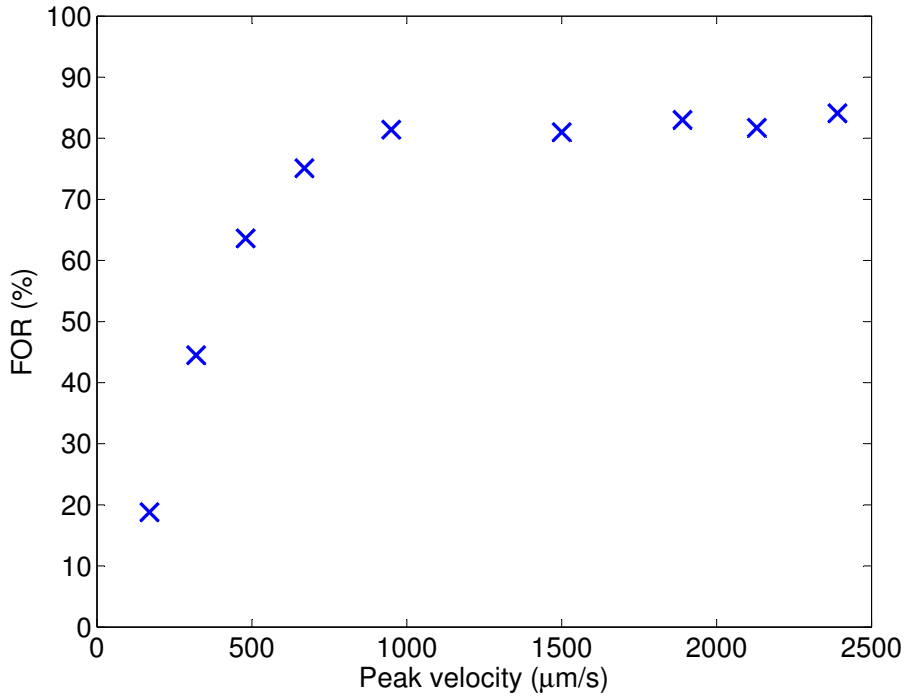

Figure 4.15: FOR for paper on loudspeaker as a function of speed, BW = 12kHz, f_{vib}=3kHz

input power of 50μW, the power on the detector will be 105nW (100nW from reference arm and 5nW from the measurement arm) instead of 200nW (equal power in both arms). The SNR will be still limited by the relative intensity noise of the current drive for this power level (Fig. 4.10). However, the power is now not equally divided into both arms and this will result in a SNR penalty of 4dB (SNR=36dB) and consequently a 4dB higher noise equivalent speed. This is what we also observe during measurement. The shot noise limited SNR is for these power levels 50dB, still 14dB higher than what we achieved. The FOR for sound on the loudspeaker with vibration frequency of 3kHz is given in Fig. 4.15. In comparison with the retroreflective film, a speed of 500μm/s for a FOR of 60% is needed instead of 300μm/s. For a FOR of 80% a speed of 1000μm/s is necessary instead of 800μm/s.

4.5 Conclusion

In this chapter, we build a fiber based heterodyne LDV. It is computer connected to demodulate the signal. The OFS is realized by means of serrodyne frequency shifting with an electro-optic phase modulator. The input polarization to the phase modulator should be done carefully to obtain sufficient side mode suppression. If this is the case, side mode suppression can be as low as 33dB, which corresponds with a modulation error smaller than 95%.

It turns out that the SNR is not limited by shot noise, but rather by the noise on the drive current of the laser. The highest SNR* we can get with the lowest possible power on the detector is around 40dB for 200nW with equal power in the interferometer arms. This is when a retroreflective film is put on the vibrating object under test and a 99:1 splitter after the laser is used. 50μW is then send into the input of the LDV. We measure a corresponding noise equivalent velocity of 100μm/s for a bandwidth of 12kHz, in correspondence with calculations. With these power levels, we are 15dB in SNR* away from shot noise limited operation. If we compare our vibration measurements with results from a commercial available LDV, the shape of the signals correspond well. However, there is a difference in amplitude of the signal by a factor 0.76. If we take this factor into account, the resemblance between both signals can attain 90% for speeds on the order of 10 times the noise equivalent speed. For too high speeds, part of the FM spectrum falls outside our bandwidth and resemblances drops again. A higher bandwidth can then be used, but then also the noise equivalent speed rises.

To imitate the extra losses we can expect when measuring on a bone in the middle ear, we replaced the retroreflective film with a piece of paper. This causes extra losses of 13dB. Because we now deviate from the ideal scenario where power is equal in the arms, we pay a power penalty of 4dB and the noise equivalent speed rises accordingly.

Chapter 5

Conclusions and future outlook

5.1 Conclusions

In this master thesis we explored the potential of photonic integration technologies for LDV-based hearing implants. In the first part, we discussed different detection methods for measuring the Doppler shift. The heterodyne detection is the option with the least noise involved. We derived also a fundamental limit on the performance of the LDV. This derivation is based on shot noise, which is inevitably present at the conversion between photons and electrons. Calculations show that the optical power arriving at the detector should be higher than 100mW to fulfill the requirements for the optical microphone. This is 100 times above the power budget for an implantable hearing implant.

Next, we searched for a possible outlook of an integrated heterodyne LDV on SOI. Integrated lasers and detectors can be produced, but integrated optical frequency shifters are not readily available. We proposed to use serrodyne frequency shifting: the shifting is then realized by a sawtooth phase modulation. Imperfections in this modulation will cause spurious sidebands. The sideband at the negative of the desired frequency shift results in an error of the measurement. Therefore, this sideband should be kept as low as possible.

A proof-of-principle implementation was built in fiber. It is in fact a macroscopic version of the integrated version. The fibers can be seen as an analogue of the waveguides;

an electro-optic phase modulator realizes the serrodyne frequency shift. The signal is brought to a computer, where demodulation takes place. The serrodyne frequency shift is evaluated and it is found that a modulation error smaller than 95% can be achieved when the polarization input is well adjusted.

We measured the vibration of a retroreflective film on a loudspeaker. A noise equivalent speed of 100μm/s was seen for a bandwidth of 12kHz and power of 200nW on the detector, which is 15dB above shot noise limited operation. The main noise source was found to be the noise on the current driving the laser. Improvements like a more stable current source or balanced detection will lower the noise equivalent speed. Comparison of our measurements with those made with a commercial LDV reveal that the shape of both match well for velocities well above the noise equivalent speed. However, there is an amplitude error which is treated as a calibration factor in the rest of the measurements.

Finally, we performed measurements on a weakly reflecting piece of paper. The lower power we get back from this (13dB lower), leads to a drop in the signal to noise ratio and eventually a higher noise equivalent speed (4dB higher).

5.2 Future outlook

Our proof-of-principle implementation was able to be used as vibration sensor. The possibility exists to implement this fiber LDV as a miniaturized version in the future. All components used in the fiber LDV are also available in SOI format. Laser and detector can be inserted by bonding technologies, the OFS can be realized by serrodyne phase modulation. Carrier injection seems a good option, since it has high bandwidth and will create only small sidebands.

The smallest vibration displacements to be measured in the middle ear are on the order of pm. This imposes high power specifications, even in shot noise limited operation. This in conflict with the limited power budget of a hearing implant. However, there may be other fields where a miniature vibration sensor with less stringent requirements can be used.

Bibliography

[1] G. Roelkens, L. Liu, J. Brouckaert, J. Van Campenhout, F. Van Laere, D. Van Thourhout, and R. Baets. Wafer bonding and heterogeneous integration: III -V/silicon photonics. In *14th European Conference on Integrated Optics and Technical Exhibition. Contributed and Invited Papers*, pages 87–90, 2008.

[2] G. P. Agrawal. *Fiber-optic Communication Systems*. Wiley-Interscience, third edition, 2002.

[3] P. Gren, K. Tatar, J. Granstrom, N.E. Molin, and E.V. Jansson. Laser vibrometry measurements of vibration and sound fields of a bowed violin. *Measurement Science & Technology*, 17(4):635–644, Apr 2006.

[4] S. Weissner and F.E. Talke. Load/unload measurements using laser doppler vibrometry and acoustic emission. *Triboloby Internation*, 33(5-6):367–372, May-Jun 2000.

[5] E. M. Lawrence, K. E. Speller, and D. Yu. Mems characterization using laser doppler vibrometry. volume 4980, pages 51–62. SPIE, 2003.

[6] N. Xiang and J. M. Sabatier. An experimental study on antipersonnel landmine detection using acoustic-to-seismic coupling. *The Journal of the Acoustical Society of America*, 113(3):1333–1341, 2003.

[7] S.M. Khanna, J. Tonndorf, and W. W. Walcott. Laser interferometer for the measurement of submicroscopic displacement amplitudes and their phases in small biological structures. *The Journal of the Acoustical Society of America*, 44(1):357–357, 1968.

[8] S.M. Khanna. Homodyne interferometer for basilar membrane measurements. *Hearing Research*, 23(1):9 – 26, 1986.

[9] P. R. Dragsten, W. W. Webb, J. A. Paton, and R. R. Capranica. Light-scattering heterodyne interferometer for vibration measurements in auditory organs. *The Journal of the Acoustical Society of America*, 60(3):665–671, 1976.

[10] Y. Yeh and Hz. Cummins. Localized fluid flow measurements with an He-Ne laser spectrometer. *Applied physics letters*, 4(10):176, 1964.

[11] P. Horowitz and W. Hill. *The art of electronics*. Cambridge Univ. Press, Cambridge, 1980.

[12] J. R. Carson. Notes on the theory of modulation. *Proc. IRE*, 10(1):57–64, 1922.

[13] T. Suzuki and R. Hioki. Translation of light frequency by a moving grating. *J. Opt. Soc. Am.*, 57(12):1551–1551, 1967.

[14] H. Cummins, N. Knable, L. Gampel, and Y. Yeh. Frequency shifts in light diffracted by ultrasonic waves in liquid media. *Applied Physics Letters*, 2(3):62–64, 1963.

[15] R. E. Best. *Phase-locked loops: Design, Simulation and Applications*. McGraw-Hill, 2003.

[16] J. J. Carr. *RF components and circuits*. Elsevier, 2002.

[17] J. S. Chitode. *Communication Engineering*. Technical Publications, 2009.

[18] P. De Heyn. A compact optical frequency shifter using a multi-branch waveguide interferometer. Master's thesis, University of Ghent, 2009.

[19] R. Baets Y. Li, S. Meersman. Optical frequency shifter on soi using thermo-optic serrodyne modulation. unpublished, 2010.

[20] William M. Green, M. J. Rooks, L. Sekaric, and Y. A. Vlasov. Ultra-compact, low rf power, 10 gb/s siliconmach-zehnder modulator. *Opt. Express*, 15(25):17106–17113, 2007.

[21] L.M. Johnson and C.H. Cox. Serrodyne optical frequency translation with high sideband suppression. *Journal of Lightwave Technology*, 6(1):109 –112, jan 1988.

[22] M. Lawrence. Lithium-niobate integrated-optics. *Reports on Progress in Physics*, 56(3):363–429, Mar 1993.